Optical Studies of Indium Gallium Nitride Nanostructures

by

Adam Katcher

A dissertation submitted in partial fulfillment
of the requirements for the degree of
Doctor of Philosophy
(Physics)
in The University of Michigan
2018

Doctoral Committee:

Associate Professor Hui Deng, Co-Chair
Associate Professor Pei-Cheng Ku, Co-Chair
Professor Roy Clarke
Associate Professor Emmanouil Kioupakis
Associate Professor Vanessa Sih

Adam Katcher

akatcher@umich.edu

ORCID iD: 0000-0003-3967-0055

Dedication

In memory of my grandfather, Theodore

Acknowledgements

First and foremost, I give my deepest appreciation and thanks to my advisor, Hui Deng. Hui welcomed me into her research group and gave me access to the things I needed to complete my PhD. Our work together and Hui's careful questions to test my understanding as well as guidance about experimental matters have been a critical aspect of my training as a physicist.

Thank you to PC Ku, who is co-chair on my committee and whose group were our close collaborators. In addition to the work of his group fabricating and continually developing the InGaN nanostructures samples studied in my thesis, PC also provided very useful input and guidance during our meetings and always knew the next steps to move a project forward.

Deep thanks go to Roy Clarke, Emmanouil Kioupakis, and Vanessa Sih for agreeing to serve on this defense committee and offering their experience and expertise.

The Deng group members have been excellent colleagues. Special thanks to the nitride group: Lei Zhang for his important early work on InGaN QDs before I joined the group, Tyler Hill for helping to train me and offering research guidance, and Eunice Paik for her valuable work in the lab. I would also like to thank the members of PC Ku's group, including Chu-Hsiang Teng, Kunook Chung and Jingyang Sui for their impressive work and valued collaboration. Special thanks to Brandon Demory for his leadership and collaborative spirit on several projects.

I would like to thank Duncan Steel and his group members for having me in their group when I started graduate school and for their comradery, in particular Aaron Ross for always being around to share ideas about optics experiments and troubleshooting.

Teaching has been an important aspect of my experience during the course of this work. I thank the professors with whom I have worked, including members of this committee as well as Ramon Torres-Isea and Carl Akerlof who help make the undergraduate physics labs world-class.

I would also like to thank the Department for its collegial environment and its support of its graduate students. Special thanks to grad chair Vanessa Sih and previously Finn Larson, student services staff including Chrissy, Nitesh, Elise, and facilities staff including Paul and Joe who keep the labs running smoothly.

Thanks to my Ann Arbor friends, in particular Alex and Thomas for being great roommates for four years.

Thank you to Johanna for believing in me and for cooking meals together so that I am not only subsisting on burritos. Finally, thank you to my family for their abiding encouragement of my education throughout my life.

Table of Contents

List of Figures

Abstract

Indium gallium nitride (InGaN) is a semiconductor material that is in widespread use in blue light emitting diodes (LEDs) and blue laser diodes and is being used in solid-state lighting, displays, and scientific applications. The scientific understanding of the physical mechanisms responsible for the performance of these devices is still developing; this includes the description of localization of carriers in this material – a fundamental issue which is believed to be responsible for the origin of luminesce in blue LEDs – as well as that of performance limitations of existing devices, including the so-called "green gap" and "efficiency droop," which are related in part to the exciton-phonon interaction. This thesis studies top-down etched InGaN quantum disks (QDs) embedded in GaN nanopillars, focusing on the effect of localization and of the exciton-phonon interaction.

The exciton-phonon interaction is studied with two experiments which examine the effect of quantum dot size and shape on the strength of the optical phonon replica in the PL. First, we study the effect of asymmetrical strain on the exciton-phonon coupling by examining the optical phonon replica in the PL of nineteen individual elliptical QDs with dimensions of 22nm x 36nm. We show that the effect of strain on the phonon coupling strength should be observable by a reduction in the degree of polarization (DOP) of the optical phonon replica. Measurements confirm that there is a reduction in the DOP of the optical phonon replica, with reasonable agreement with theory for the high DOP dots. Lower DOP dots, which arise to due irregularities in the shape and

size of the fabricated nanopillars, also show a reduction in DOP of the phonon replica but are more sensitive to the effect of asymmetrical phonon coupling and warrant further study. Second, we examine the effect of nanopillar diameter on exciton-phonon coupling strength in InGaN quantum disks. We observe an enhancement of the phonon replica as the nanopillar diameter is reduced from 1000nm to 60nm. This effect is explained by a reduction in the lateral Bohr radius of the exciton which accompanies the decrease in vertical electron-hole separation in smaller nanopillar diameters. To quantify this effect, a simple model is used to infer that, based on the measured phonon coupling strengths, the Bohr radius reduces from approximately 2.5nm to 2nm as the diameter is reduced over the observed range.

In order to study the effect of localization, we measure the Stokes shift, which is the energy difference between emission and absorption. By measuring this quantity as a function of nanopillar diameter, we demonstrate the ability to separately determine the contributions of the strain-induced quantum confined Stark effect and of localization to the observed Stokes shift. In our case, we find that the two effects have approximately equal contributions for the range of nanopillar diameters studied here.

Furthermore, the site control of InGaN/GaN quantum disks using this top-down fabrication method assists the integration of advanced device structures with individual nanopillars. We demonstrate the enhancement of light collimation by a factor of 1.8x from single nanopillar LEDs using an integrated nanolens. Additionally, we report measurements of enhanced QD brightness and radiative emission rate using an open-top plasmonic cavity; this demonstration is tailored for applications in quantum technologies such as quantum cryptography.

Chapter 1
Thesis motivation and summary

Despite the widespread use of InGaN-based devices including blue LEDs and laser diodes, understanding about the physical mechanisms of their operation is still lacking. This understanding will enable the scientific community to overcome the observed limitations of existing technologies and to develop new functionality that will enable future applications including quantum technology. This thesis presents studies of InGaN quantum disks embedded in GaN nanopillars, focusing on using experimental optical measurements to understand the underlying physics relating to the interplay of localization, strain, and phonon coupling strength in this material. In order to introduce the motivation of this work, in this chapter we discuss the current state of affairs of applications of InGaN light emitters in four sections. In section 1.1, we introduce the basic concept of InGaN LED technology, followed by a description in 1.2 of why InGaN LEDs are an advantageous material for the application of solid-state lighting. In section 1.3 we describe applications of InGaN light emitters in the realm of quantum technology. Finally, section 1.4 describes problems in the field, including device limitations known as the "green gap" and "efficiency droop," and the fundamental issue of localization of carriers in this material. Finally, section 1.5 gives an outline of the remainder of this dissertation.

1.1 Light emission in InGaN

Light emission in semiconductors is controlled by the energy levels of the system. Light emission in a semiconductor can occur when an excited electron in the conduction band radiatively recombines with a hole in the valence band, with the energy of the emitted photon influenced by the bandgap separating these two energy bands. GaN has a wide bandgap, whose value at low temperature is approximately 3.5 eV (for wurtzite GaN) [1]. Meanwhile, InN has a much smaller value of the bandgap, approximately 0.7 eV [2]. With GaN emitting in the UV and InN in the IR, $In_xGa_{(1-x)}N$ alloys with varying indium fraction x emit light that spans the visible spectrum.

Furthermore, in a QW, there is a bandgap discontinuity at the interface between InGaN and GaN, thus creating a potential well which provides confinement to carriers in the well. The potential profile in a QW generates bound states within the well, in analogy with the textbook quantum mechanics example of a particle in a box (a more accurate description is given in later chapters). Confinement of electrons and holes increases the efficiency at which the injected electron-hole pairs recombine into emitted photons. A basic schematic showing light emission in a QW is shown in Figure 1.1.

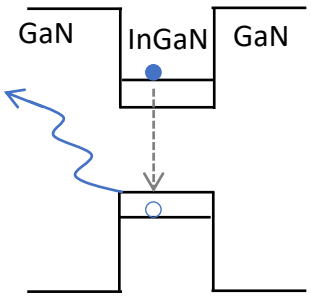

Figure 1.1: Concept of light emission in an InGaN quantum well.

The importance of nitrides arose historically due to the lack of an efficient light emitter in the blue spectral range. While red and green emitting LEDs based on GaAs/AlGaAs, GaP/AlInGaP and GaAs/AlInGaP had been previously developed, the blue LED was not widely available until

the discovery of how to use InGaN as an LED material. Blue LEDs are particularly important because they can be downconverted to other longer wavelengths using phosphors. In this way, the discovery of the use of InGaN as a blue light emitter also opened the door to efficient generation of white light.

High quality nitride materials began being fabricated when it was discovered how to use AlN and GaN nucleation layers upon which smooth GaN surfaces could be grown. Furthermore, the development of LED and laser diode technology is based upon the requirement to create n and p doped materials. In a p-n junction of an LED, p-type and n-type layers inject carriers (holes and electrons) into the active layer where they radiatively recombine to emit light, as shown in Figure 1.2.

While doping may sound a trivial matter, the ability to dope at a level of $10^{16}/cm^3$ represents a precision of some six or seven orders of magnitude as compared to the atomic concentration (density) of the bulk material. The n-doped was achieved readily using Si, yet in the early history of developing the nitride LED, the challenge of achieving p-doping of GaN blocked progress in developing the technology. Eventually, p-doping with Mg was achieved. It was discovered that for Mg to act as an acceptor, bonds between Mg and Hydrogen must first be broken, which was achieved using annealing in nitrogen [3]. With this breakthrough, in 1993 Nakamura demonstrated the first blue LED with high brightness, thus opening the door for practical applications. This work was rewarded with the Nobel Prize in 2014 to Akasaki, Amano, and Nakamura.

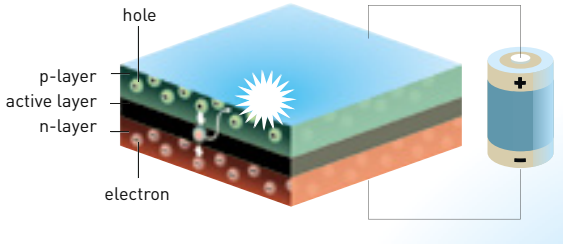

Figure 1.2: LED light emission. Image from [2].

1.2 LED lighting

The early uses of LEDs were applications such as small indicator lights. Developing LEDs for general illumination and for display technologies requires consideration of the emitted spectrum. For lighting applications, a broad spectrum is required in order to properly illuminate a scene. Likewise, white LEDs are used as backlights of liquid crystal displays (LCDs) which consists of an array of pixels for which the transmission is individually tuned. Thus, in both cases white light is required. The typical solution is the use of a phosphor such as Ce:YAG. Typically, a yellow phosphor could be used (typical peak emission near ~560nm) with a broad bandwidth (a typical full-width-at-half-max being comparable to 100nm), and with quantum efficiency of 85% [4]. This approach offers a degree of color mixing that gives phosphor-converted LEDs a white appearance. However, the color-mixing only of the narrow blue LED emission and broad yellow is insufficient to cover the full color gamut. To achieve a full color spectrum, or even simply to create a warmer white light, red and green phosphors could be used. Unfortunately, phosphor-converted emission results in energy loss in the phosphor. The alternative to phosphor-converted LEDs is to use "color-mixing" whereby LEDs of several different emission wavelengths are combined in order to approximate the desired spectrum. Additionally, applications such as micro-displays require small form factors. In this way, RGB LEDs are also useful for displays.

It is well known that LEDs present a clear advantage in lighting. As compared to incandescent bulbs, they are vastly more efficient. At the root of this efficiency is the nature of the emission process. LEDs are solid state light emitters and emit with a typical bandwidth of tens of nm at an energy directly visible by the human eye, as compared to the incandescent bulb whose peak energy is of course in the IR with a tail that extends into the visible. It is for this reason that commercially available, inexpensive LED bulbs are about 10x more efficient than incandescent

(160 lm/W vs 15 lm/W), with demonstrated LED efficiencies even twice as high as that [5]. The maximum luminous efficacy is by definition 683 lm/W for monochromatic green light at the peak responsivity of the human eye, and the maximum possible value for "white" light is around 300 lm/W but depends on the exact spectrum of the light. Thus, commercially available LEDs are already within a factor of 2x or so from the limit of luminous efficiency, with laboratory demonstrations already proving this gap can be narrowed. However, as we will explain shortly, these efficiencies must be expanded to higher injection currents and to samples with higher indium concentration.

Because of their enhanced efficiency, one of the goals of developing this technology is to reduce energy usage. This goal has major implications, as lighting alone accounts for 16% of the world's electrical energy expenditure [6]. Interestingly, it is difficult to predict to what extent an increase in efficiency will actually translate into decreased energy expenditure, because it is quite possible there could be a "rebound effect" in which a lower cost is accompanied by more usage [7]. Whatever the commercial and societal results, the development of LED lighting has enormous influence on society. With lighting a $350B/year industry – this was a 2005 global estimate which includes about $230B of energy usage and the remainder equipment and labor costs – it seems clear there is room for enormous growth of InGaN LEDs [8].

GaN is now considered the second most industrially important semiconductor material after Silicon, with a market size of $15 billion / year, exceeding that of GaAs [9]. A large segment of this is based on the role of GaN in solid state lighting. Low-dimensional InGaN/GaN heterostructures are central to the future of the solid-state lighting industry as well as providing promise for quantum photonic technologies. Additionally, nitride materials are being used in high-power electronics.

1.3 Quantum technologies

The use of wide bandgap materials also has applications in quantum technology including quantum cryptography and computation. Quantum cryptography seeks to use single photons to encode messages whose privacy can be ensured by the randomness inherent to measurements of quantum states. Quantum computation makes use of quantum states to encode information and implement quantum algorithms which are believed to be more computationally efficient that any classical algorithm for solving certain problems such as prime factorization.

Single photons cannot be generated by simply attenuating a traditional light source down to low levels. In that case, the photon number distribution is merely shifted toward an average number of one, but there is still large probability of zero or two photons. Instead, a single photon may be generated by radiative recombination of a single electron and hole. However, typical materials do not facilitate excitation of a single exciton at a time. In a quantum dot, a small island of a low bandgap material is embedded in a matrix of a material of larger bandgap. This creates confinement in all directions; for this reason, quantum dots are referred to as zero-dimensional systems. They have also been referred to as artificial atoms due to the quantized energy eigenstates that arise from the confinement.

Thanks to the confinement in a quantum dot, it is possible to excite a single exciton at a time. In this way, QDs can act as a single photon source. This feature is attributable to the biexciton binding energy in a QD. Even with non-resonant excitation, the interaction between two excitons means that the energy of two excitons does not equal twice the exciton energy, thus allowing only single exciton emission to be spectrally selected with a filter. In most materials, the biexciton is lower in energy than the exciton, as the carriers rearrange themselves such that the attractive energy

between oppositely charged carriers exceeds the repulsion between like charges. Notably, in nitrides, in some cases a negative biexciton binding energy has been observed; this situation has

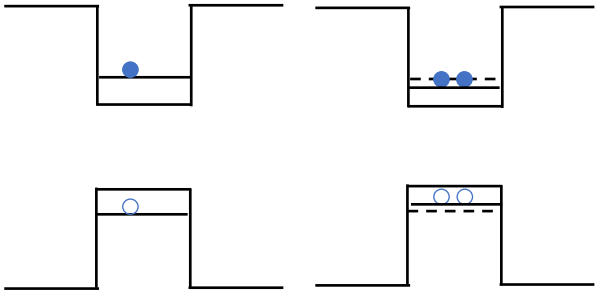

Figure 1.3: Exciton and biexciton states in a QW with a positive biexciton binding energy.

been attributed to the large piezoelectric fields which inhibits the spatial separation of like charges.

In the past, most of the demonstrations of these technologies have used nanostructures of narrow band gap materials such as GaAs which can be fabricated with pristine quality. However, the performance of these materials is inherently limited to low temperatures, typically 5K. In contrast, wide-bandgap materials such as InGaN alloys (with relatively low indium concentration) are operable at higher temperatures. This higher temperature application arises in large part from the enhanced exciton binding energy. This fact allows excitons to exist in InGaN without dissociating at higher temperature.

Developments in quantum information science are now being moved into the commercial realm. Most of these efforts are focused on building quantum computers with tens or hundreds of qubits, with many efforts being made using superconducting qubits. These developments are encouraging and indicate that hopefully within a decade simple algorithms could be implemented on these systems which would offer computational speeds faster than any known classical algorithm, an achievement known as “quantum supremacy.” While superconducting qubits are currently leading the way, these typically require millikelvin temperatures provided by a dilution

refrigerator, which results in bulky and expensive setups. For this reason, higher temperature qubits, for example based on InGaN QDs, are worth exploring in order to make the technology more scalable. However, InGaN as a material for quantum computation is still in its infancy, with only very early attempts to demonstrate the coherence properties required for a quantum computation application [10].

1.4 Ongoing areas of study in InGaN

We now discuss several issues regarding InGaN which have relevance to this thesis. These include localization, defect density, the green gap, efficiency droop. Finally, we briefly note the topic of the health effects of solid state lighting; although this topic is not directly relevant to the work described in the following chapters, it may inform the future of technology development as much as the any of the other technical issues facing the field.

1.4.1 Localization

Another approach to addressing efficiency droop and to understanding nitrides is to better understand the broader question of the mechanism of localization. It is well known that despite the presence in InGaN of a defect density that is six orders of magnitude greater than that of other materials, it nonetheless has a high IQE and is a practical light emitting material. The size of the localization was determined to be 1-3nm using the intensity of phonon sidebands in the PL [11].

Early on, it was hypothesized that gross clustering of indium provided a ready explanation for the origin of the hypothesized localization centers; the electrons and holes would become trapped in the In-rich clusters due to their lower bandgap. This would enable bright luminescence when the exciton remained localized over timescales longer than the radiative lifetime. This theory

was presented early on which suggested the occurrence of In clustering and even pure InN QDs [4] [12].

The indium clusters were hypothesized to be small enough to typically avoid the spatial locations of the dislocations, facilitating the localization of excitons away from high density of defects (a reported value of the dislocation spacing is around 300nm [13]). This hypothesis was at the time supported by electron beam microscopy which appeared to image indium clusters [2]. The existence of indium clustering was also motivated by theoretical investigations regarding a possible miscibility gap [13]. However it was demonstrated that the electron beam images were artifacts due to damage to the samples from the electron beams, and the updated careful measurements showed no evidence for gross indium clustering [13]. Thus, it was realized that pure InN clusters were not the cause of localization, and this situation reignited the search for a different cause of the efficiency droop.

At this time, gross indium clustering is not believed to exist in most InGaN samples. In fact, the fluctuations in indium content are believed to typically be that expected from a pure random alloy [13]. Thus, it is believed there must be some other mechanics for the localization of excitons in GaN.

Today, the main mechanisms of localization considered to be relevant in InGaN QWs are well width fluctuations, indium concentration fluctuations due to random alloying, or possibly even localization at In-N-In chains [14], [15]. Motivation into understanding localization regards not only the fundamentals of the mechanism of light emission in InGaN, but also may inform further improvements. For example, localization due to indium fluctuations have been demonstrated theoretically to enhance Auger recombination, in which the electron and hole energy is transferred to a third charge carrier as opposed to emitting a photon [16]. Additionally, these

studies also address the question of whether light emission arises from excitons or from separately localized electron and holes [11] [17].

The nature of localization has been studied using temperature dependent PL measurement which indicate an "S-shaped" emission energy with respective to temperature. At the lowest temperatures, there is a redshift with increasing energy as it is believed that the thermal energy allows carriers enough kinetic energy to find deeper potential minima. This is followed by a blueshift as carriers are believed to be able to occupy higher energy states. And finally, there is another redshift beyond 150K due to the reduction of bandgap with temperature. Additionally, time resolved PL have been used to determine the dynamics of recombination in order to understand the role of localization.

1.4.3 Green gap

Besides the general question of the origin of luminescence and the role of localization, there are several other important questions about InGaN LED performance [18].

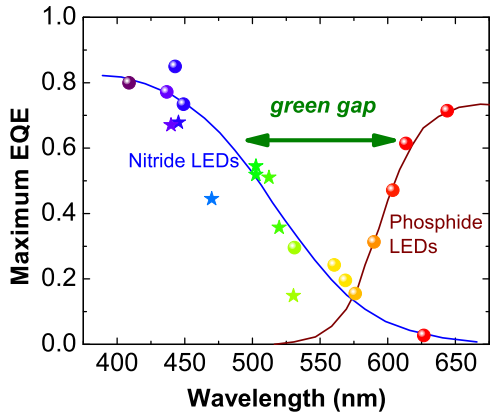

Figure 1.4: Green gap in LED technology. Image from [19]

One issue regarding InGaN LED performance is the "green gap." This refers to the lack of an efficient green-emitting LED material. InGaN currently offers efficient LED performance in the violet and blue spectral range, and InGaP and other materials offer efficient red LED emission. Of course, InGaN with higher In concentration should serve as a green LED. For reasons believed to be related to Auger recombination, green-emitting InGaN suffers from lower quantum efficiency [19]. Much work has gone into explaining the origins of the reduced efficiency of green-emitting InGaN.

A factor influencing the green gap may be that in samples of higher indium content, the piezoelectric fields are greater, thus reducing the electron-hole wavefunction overlap and increasing the radiative recombination time. Because the radiative recombination competes with nonradiative recombination, the extensions of radiative recombination time also results in lower efficiency. Another contributing factor to the reduction of efficiency with increasing indium concentration may be reduced crystal quality. Finally, it is believed that a major factor causing the green gap is an increase in Auger recombination arising from the increase in Indium concentration [19].

1.4.4 Efficiency droop

Another area of interest regarding InGaN LED performance is the reduction of efficiency at higher levels of current density, a problem referred to as "efficiency droop". In terms of commercialization of LEDs, the conversion efficiency from electrical energy to light energy is itself not a sufficient condition to create an affordable product. In addition to efficiency, the devices should ideally be small - both for practical purposes and to use less InGaN material - and must produce a lot of light. Thus, there is a need to drive the LED at a higher current density. It is

observed that at these higher current densities, the efficiency drops. Early on, Nakamura theorized that efficiency droop arose from saturation of the localization centers. Much effort has gone into explaining this effect and exploring methods to alleviate the problem.

Generally speaking, the problem of efficiency droop is not solved but has been attributed to the high defect density and is related to localization, as well as to Auger recombination. While localization is believed to protect carriers from defects at low current densities, this does not seem to remain true at higher current densities. One approach to alleviate the efficiency droop is thus to grow InGaN materials with a lower defect density. Improved understanding of the mechanism of efficiency droop will inform the solutions.

An important result in this area was [20], which presented a measurement of Auger coefficients and suggested that this mechanism was responsible for the efficiency droop. [21] determined several aspects about efficiency droop including its temperature dependence. Namely, it was believed that the droop could be due to heating at higher injection current densities, but this paper in fact revealed the opposite trend of less droop at higher temperatures. However, this study did not attribute the droop to Auger recombination. Following this, [22] made more direct observations that substantiated the assignment of efficiency droop to Auger recombination. These ideas continue to be investigated.

1.4.5 Health effects of solid state lighting

Although we do not directly address this issue in this thesis, the health-related issues regarding lighting are also beginning to motivate the functionality of LED technology. Because solid state lighting is often generated by a blue LED pumping a yellow phosphor, the emission spectrum is of course not as smooth as that of other light sources such as sunlight. Instead, in the blue spectral range the spectrum consists of a very narrow and bright blue peak.

Nakamura has recently commented on the health concerns of solid state lighting. In a talk at University of Michigan, Nakamura discussed the potential effects of blue light on health, which are related in part to the disruption of melatonin. To confront this issue, Nakamura has suggested replacing the blue LEDs in solid state lighting with violet LEDs. These LED sources should still be effective at pumping the phosphor and creating an approximately white spectrum. This approach is now being commercialized, and its effectiveness will need to be examined.

These issues, as well as the need to apply InGaN light emitters to a variety of applications, motivate the development of new InGaN devices and an improved understanding of the underlying physics so that its light emission properties and functionality can be readily adapted to these challenges.

1.5 Thesis overview

This thesis presents optical studies of InGaN nanostructures which enhance our understanding of the fundamental optical properties of this material. The physical explanations of the observed optical properties focus on the interplay of strain, localization, and phonon coupling. We do not directly investigate the particular application questions introduced in the previous section such as the green gap or efficiency droop, in that we are not studying samples of varying indium concentration or increasing the current densities in LED devices. Rather, the answers to these questions and the design of future applications will be informed by the knowledge of the underlying physics developed in studies such as this.

This thesis studies top-down etched InGaN quantum disks embedded in GaN nanopillars. These structures are tremendously useful for controlling and studying the physics related to light emission in the system.

After a description of some of the background physics in Chapter 2, our main results are reported in five chapters. Chapters 3-4 present optical measurements of new devices which demonstrate the integration of advanced device structures with individual nanopillars. In Chapter 3, we demonstrate the enhancement of light collection from single InGaN nanopillars using an integrated nanolens. In Chapter 4, we report measurements of enhanced QD brightness and radiative emission rate using an open-top plasmonic cavity. Chapters 5-7 present experimental optical studies of InGaN nanopillars which permit an understanding of the role of strain, localization, and phonon coupling in this system, as we now summarize.

In chapter 5, we describe the effect of nanopillar shape on the exciton-phonon strength. In elliptical shaped quantum dots, the hole envelope functions associated with the x- and y- polarized emission have different spatial distributions due to the asymmetry of the x and y strain components. Thus the different hole envelope functions result in different coupling strength to the LO phonon. We observe this effect as a modification of the degree of polarization when examining the optical phonon replica in polarization-resolved photoluminescence of single InGaN QDs. The dominant component of the hole ground state corresponds to polarization aligned with the long axis of the ellipse. The reduced degree of polarization of the phonon replica arises due to an enhancement of the exciton-phonon interaction of the cross-polarized envelope function. Using nextNano calculations of each of the eigenstates, we calculate the resulting phonon coupling strength as measured by the Huang-Rhys factor and confirm that that the phonon coupling strength is theoretically enhanced by 8%.

In chapter 6, we present experimental measurements of the strength of the phonon replica in the PL spectra as a function of nanopillar diameter. This work is relevant to understanding of the effect of nanopillar size on exciton-phonon interaction. Understanding of exciton phonon interaction is a fundamentally important endeavor and relates to understanding of indirect Auger recombination, which plays a role in the efficiency droop and green gap. We observe an increase in phonon coupling strength with decreasing nanopillar diameter, which we attribute to a decrease in the Bohr radius arising from the enhanced Coulomb interaction in the smaller nanopillars. We use the measured phonon replica strengths, together with a simple model of the wavefunctions and of the field strength, to determine the in-plane localization length lambda, which defines the Bohr radius of the exciton. We find that lambda decreases from ~2.5 nm to 2nm as the diameter is reduced from 1000nm down to 60nm. This result provides an indication of the effect of the lateral potential profile - introduced by the strain tuning in these nanopillars - on influencing the Bohr radius in this material.

Finally, in Chapter 7 we carry out PLE measurements in order to measure the Stokes shift as a function of nanopillar diameter. The Stokes shift is the energy difference between the effective bandgap and the PL emission energy. Previous studies have examined the stokes shift in order to understand its origin as arising from both piezoelectric fields and from the localization depth. Because our nanopillars are adjacent to one another and are etched from a single QW, they have roughly similar indium concentration and fluctuations and so the main tuning parameter across different nanopillars is the piezoelectric field strength. Thus, by measuring the Stokes shift as a function of nanopillar diameter we can observe the effect of this piezoelectric field tuning on the observed Stokes shift. This provides evidence regarding the relative importance of indium fluctuations and piezoelectric fields in creating the Stokes shift.

Finally, in Chapter 8 we offer a conclusion to the thesis and describe proposed next steps.

Chapter 2
Properties of InGaN

In order to address the physics questions introduced in Chapter 1, we now describe some of the properties of InGaN and of InGaN disks embedded in GaN nanopillars. As mentioned in Chapter 1, the device performance of InGaN is greatly influenced by the role of piezoelectric fields. The piezoelectric fields arise from strain and spatially separate electrons and holes, causing the quantum confined stark effect which redshifts the emission and reduces the radiative recombination rate. In order to properly describe these effects, we now give a description of the origin of piezoelectric fields in this material.

2.1 Strain and lattice mismatch

The crystal structure of GaN typically occurs in hexagonal wurtzite phase. The room temperature in-plane lattice constant of wurtzite GaN is $a_0 = 0.319\ nm$ while that of InN is a = 0.355nm [1]. Because of the lattice mismatch of InGaN and GaN, this creates a lateral strain given by:

$$\epsilon_{xx} = \epsilon_{yy} = \frac{a - a_0}{a_0} \tag{2.1}$$

Here ϵ is the strain tensor and z denotes the c axis.

The compressive strain in the lateral direction results in an elongation in the vertical direction, thus creating a strain in the vertical direction. The resulting vertical strain is:

$$(\epsilon_{zz}) = \frac{c - c_0}{c_0} = -2\frac{C_{13}}{C_{33}}\epsilon_{xx} \quad (2.2)$$

Furthermore, when GaN is grown on a substrate such as sapphire, there is a strain due to the 16% lattice mismatch as well as due to thermal mismatch. This results in a high defect density of threading dislocations, with a typical density of 10^8-10^{10}/cm^2. In an InGaN/GaN QW on a sapphire substrate, the threading dislocations in GaN pass through the InGaN QW [2].

2.2 Polarization fields

Because GaN lacks inversion symmetry this results in a spontaneous polarization along the growth axis. This arises because nitrogen atoms have a greater electronegativity than do indium or gallium atoms, giving a charge asymmetry in the material. For crystal growth along the [0001] polar direction, the polarization is in the reverse direction. This direction is referred to as Ga-polar. The spontaneous polarization exists throughout both the GaN barrier layers and the InGaN QW.

Additionally, because GaN lacks inversion symmetry, any strain creates a piezoelectric polarization. In GaN, the piezoelectric constants are large and thus the piezoelectric polarization is quite huge. A large strain arises from the lattice mismatch between the InGaN QW and the barrier layers (typically GaN). The piezoelectric polarization only exists in the vicinity of the QW where the strain exists. It points opposite to the spontaneous polarization, along the growth direction. The sum of the spontaneous and piezoelectric polarization gives the total built-in polarization field. In the devices studied in this thesis, the piezoelectric polarizations are much more dominant.

This situation gives rise to the quantum confined stark effect (QCSE). The QCSE redshifts the emission energy and also reduces the wavefunction overlap, resulting in reduced efficiency. Naturally, higher indium content gives rise to greater strain and thus larger fields. Thus, QWs with

higher indium concentration are greatly redshifted, not only from the reduced bulk bandgap incurred from higher indium concentration, but additionally due to the enhanced QCSE. Similarly, a thicker well suffers from greater fields and thus the emission is redshifted. When the device is excited with many free carriers, either by optical or electrical excitation, the internal fields can be partially screened by the carriers, thus reducing the QCSE and blueshifting the emission.

As discussed in the introduction, higher indium concentration QWs suffer from lower efficiency. This performance is quantified by IQE, which measures the conversion rate of injected carriers into emitted photons. This is given by:

$$IQE = \frac{\Gamma_r}{\Gamma_r + \Gamma_{nr}} \tag{2.3}$$

In this equation, Γ_r and Γ_{nr} are the radiative and nonradiative recombination rates. As indium concentration is increased, the QCSE reduces the overlap integral thus reducing the radiative rate. To understand this, we note that the transition rate from state i to state j due to an interaction between states I and j is given to first order as [23]:

$$\Gamma_{ij} = \frac{2\pi}{\hbar} |\langle j|H|i\rangle|^2 \rho_j \tag{2.4}$$

This is known as Fermi's golden rule. Here ρ_j is the density of final states.

Thus, a reduction in the radiative recombination rate or increase in the nonradiative recombination both reduce the IQE. As the indium concentration is increased toward green and even red emission, the increase in QCSE reduces the radiative recombination rate, reducing IQE. Likewise, it is believed that with higher indium concentration, the nonradiative recombination rate is increased, for example by Auger recombination. Finally, it is also believed that greater indium

concentration results in higher density of threading dislocations, which is a major source of nonradiative recombination.

2.3 Band structure and the $k \cdot p$ method

The band structure of InGaN is relevant to the results of Chapter 5 where we use nextNano simulations to calculate approximate wavefunctions. Thus, we now introduce the concepts behind those calculations, including the $k \cdot p$ method.

Boundary conditions in quantum mechanics give rise to quantized energy levels of allowed states in bound systems. When quantum mechanics is applied to solids, this gives rise to energy bands which describe the allowed states. In direct bandgap semiconductors these states are characterized by the maxima of the valence band and the minima of the conduction band both occur at the gamma point. Above the bandgap energy, free carriers are created at a continuum of energies.

The Schrödinger equation is:

$$\left[-\frac{\hbar^2}{2m}\nabla^2 + V(r)\right]\psi_{n,k}(\boldsymbol{r}) = E\,\psi_{n,k}(\boldsymbol{r}) \tag{2.5}$$

The potential V(r) has the periodicity of the lattice. Therefore, Bloch's theorem says the solution is:

$$\psi_{n,k}(\boldsymbol{r}) = u_{n,k}(\boldsymbol{r})e^{i\boldsymbol{k}\cdot r} \tag{2.6}$$

Here, the exponential is of course a plane wave, while the eigenfunctions u have the periodicity of the unit cell. Calculating the approximate band structure can be achieved using a number of different theoretical and numerical approaches.

When the Bloch solutions are substituted into the Schrödinger equation, we obtain:

$$\left[-\frac{\hbar^2}{2m}\nabla^2 + V(r) + \frac{\hbar}{m}\boldsymbol{k}\cdot\boldsymbol{p} + \frac{\hbar^2 k^2}{2m}\right] u_{n,k}(\boldsymbol{r}) = E_n(\boldsymbol{k})\,\psi_{n,k}(\boldsymbol{r}) \qquad (2.7)$$

At k = 0, the solution is given by

$$\left[-\frac{\hbar^2}{2m}\nabla^2 + V(r)\right] u_{n,0}(\boldsymbol{r}) = E_n(0)\,u_{n,0}(\boldsymbol{r}) \qquad (2.8)$$

If the k-dependent part of the Hamiltonian is considered a perturbation, we may then apply perturbation theory to find the new eigenfunctions and eigenvalues. The proper application of such an approach to create precise and realistic solutions can be a complicated matter.

Once the bands are calculated, the curvature of the band may be used to define the effective mass. With this approximation, the electron and hole are viewed as free particles with mass given by effective mass. For GaN this for the hole, this is $m^*=0.2\ m_e$ and for In $0.07\ m_e$. Near the gamma point, electrons in the conduction band are in S-type states while the valence bands are composed to p-type states. When the strain is added into the Hamiltonian, the valence band character is replaced by linear combinations of these states.

In the case of significant carrier density inside the QW, the tilting of the band will be reduced. This may be studied by combining the Schrödinger and Poisson's equations, first using the Schrödinger equation to determine the distribution of carriers for a given electric field, then using Poisson's equation to calculate the resulting electric field for that distribution of carriers and repeating iteratively.

Chapter 3
Characterization of parabolic nanolenses on single nanopillar LEDs

In this chapter we describe our experimental work of characterizing parabolic nanolenses integrated onto single nanopillar InGaN/GaN structures comprising multicolor LED color pixels. This work was published in [24] and was completed in collaboration with Brandon Demory who performed the fabrication and simulation and with Kunook Chung who worked with Brandon on the fabrication. In section 3.1, we describe the topic of light extraction from InGaN LEDs. In section 3.2, we describe the nanolens sample and its fabrication. Section 3.3 describes the design of the experiment and its result which demonstrated the successful enhancement of light collimation with the nanolens. Section 3.4 offers a conclusion.

3.1 Light extraction from InGaN LEDs

The problem of light extraction is an important one for any InGaN LEDs device. Due to the large index of refraction of GaN ($n \approx 2.4$), the light extraction out of planar nitride LED structures into air is not very high. At normal incidence, the fraction of transmitted power is maximized, and the transmission and reflection coefficients are determined by the Fresnel equations to be:

$$R = \left(\frac{n_t - n_i}{n_t + n_i}\right)^2 \tag{3.1}$$

$$T = \frac{n_t}{n_i}\left(\frac{2\,n_i}{n_t + n_i}\right)^2 \tag{3.2}$$

Here $n_{i,t}$ are the indices of refraction of the ray in the initial material and the material being transmitted into, respectively. These equations are symmetrical in *i* and *t.* For the typical example of the air/glass interface, we have $n_i \approx 1, n_t \approx 1.5$ and we have the well-known value $R = 0.04$. For the air/GaN interface $n_i \approx 2.5, n_t \approx 1$ we obtain $R = 0.18$, $T = 0.82$. In fact, the situation is much worse than this. Away from normal incidence, the Fresnel reflectance increases, and even more light is trapped in the material, up to the critical angle at which R = 1, corresponding to total internal reflection (TIR). Thus, it is clear that a large fraction of the light will be reflected at the interface and this will limit the practical performance of the device in terms of light extraction. Furthermore, the light that does escape will cover a range of angles (considering the forward direction, the spatial emission will follow a distribution over the full 2π steradians), which may not be well-collimated enough for most useful applications. LED devices thus benefit from some means of directing the light emission along the normal direction.

We note that one approach to increase the light extraction and collimation is to use a cavity which controls the directionality of light emission. Cavity designs include photonic crystals, distributed Bragg reflectors, and plasmonic cavities. While all such approaches have their benefits, they generally increase the complexity of the device. We explore this further in Chapter 4 where we demonstrate a plasmonic cavity using silver coatings onto the nanopillars. The cavity approaches not only collect more of the emitted light, but actually modify the photonic modes of the system and thus enhance the actual recombination rate and the emitted brightness. However, if the only aim is to increase the light extraction and collimation, a simpler method may be used. In this chapter, the approach used in this study is relatively simple which is to integrate a lens onto the nanopillars.

There are a couple methods we now note which are used to affect light extraction. One simple approach is the use of surface roughening; this tends to increase scattering at the rough interfaces, thus allowing more of the light to escape the device into air. Also, it may be commonly observed that many LEDs use epoxy domes housing the LEDs, which modifies the angular distribution of the light emission, namely by collimating the light. While this is a useful feature, it of course does not increase the total light extraction from the actual planar device into air.

For that purpose, a lens must be integrated onto the surface of the sample to modify the reflectivity at the sample-air interface. This basic idea has been used previously, for example with hemispherical solid-immersion lens (h-SIL). The SIL is an approach continuing that of oil immersion for microscopy used in biology, designed to increase the light extraction by increasing the effective numerical aperture of the external collection optics. SILs have also been placed onto quantum dot samples [25]. This approach is effective but can be further optimized for individual nanoscale emitters. For a QW light emitter, because the light emission area is an extended object, a lens integrated on top of the sample will increase the light extraction, but its effect will be greatest for emitters near the center of the lens, with reduces effectiveness for emitters near the edges of the lens. In addition to this lateral alignment issue when looking at the case of an emitter such as a single QD, a traditional SIL is also not optimized to the vertical position of an individual emitter. Very importantly, a SIL, like any external optic, is relatively bulky and as with any external optics, requires manual placement and alignment onto the sample. We overcome these limitations using nanoscale optical elements, namely a parabolic nanolenses in order to collect the light emission a single nanopillar.

3.2 Nanolenses integrated onto nanopillar LEDs for microdisplays

Nanopillar structures have improved light extraction as compared to planar structures, thus our samples are already an improvement over planar InGaN QWs [26]–[29]. Furthermore, these nanopillar LEDs are useful for patterning micro-displays, with arrays of nanopillars comprise different pixels of the display [30]–[37]. Microdisplays are a technology being developed for head-mounted displays used in the burgeoning field of artificial reality/virtual reality. Our demonstration of microdisplays uses arrays of nanopillars to serve as RGB pixels, with variation of the nanopillar diameter providing the tuning to control the emission wavelength.

In addition to the benefits of integrated nanolenses over external optics mentioned previously, making external optics achromatic in order to accommodate the range of emitted wavelengths in a microdisplay will result in added complexity and likely increased cost and bulkiness. Thus, nanolenses fabricated nanopillars are a promising means of enhancing the light collection and collimation for microdisplays. Here, we demonstrate the integration of the lens onto single nanopillars.

In this study we use nanopillars etched from MQWs with 5 periods, thus a single nanopillar contains 5 QDs. This is done in order to increase the brightness of the sample to facilitate easier demonstration of the effect. The design and fabrication of the devices was done by Brandon Demory and Kunook Chung. To fabricate electrically injected samples, metal contacts are required (furthermore, the starting wafer consists of doped GaN layers whereas this is not necessary purely for optically pumped samples). To create the contacts, an insulating layer of SiN is developed using PECVD and is planarized with spin on glass (SOG). The SOG and SiN are removed from the nanopillar top surface using wet etching. Ni/Au (8nm/8nm) contacts are used, with the Ni adhering better to the sample surface than does pure Au. The lenses are made of SiN, which has an index of 2.0. The nanolenses are 1um in diameter and 500nm in height, with a parabolic shape

designed to be well focused for QD emission approximately 250nm below the nanolens (inside the nanopillar). The lens is formed with the desired shape and position using a resist-reflow process [24].

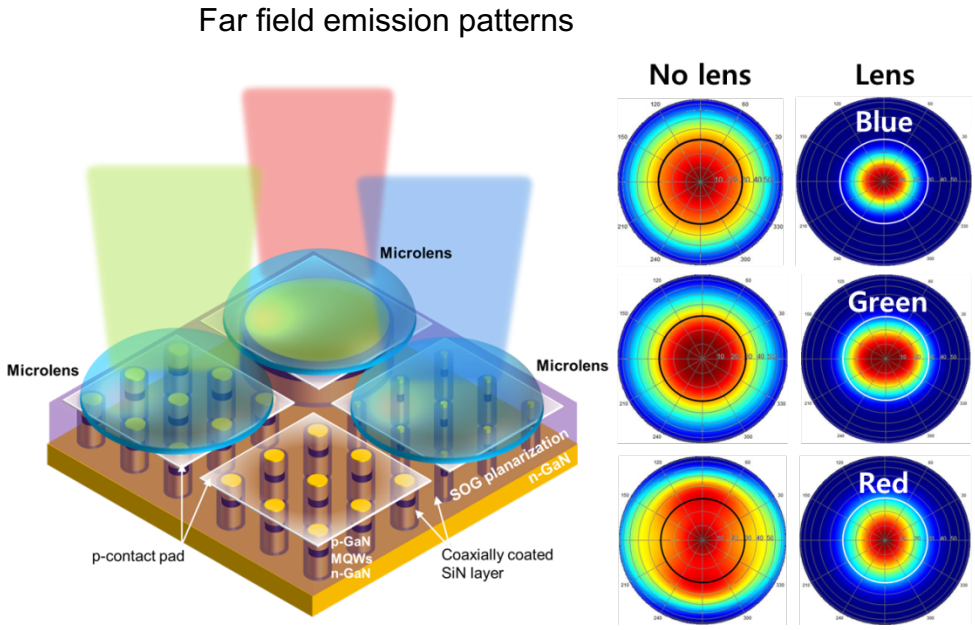

Figure 3.1: Schematic of the nanolens concept and simulated far-field emission patterns. .

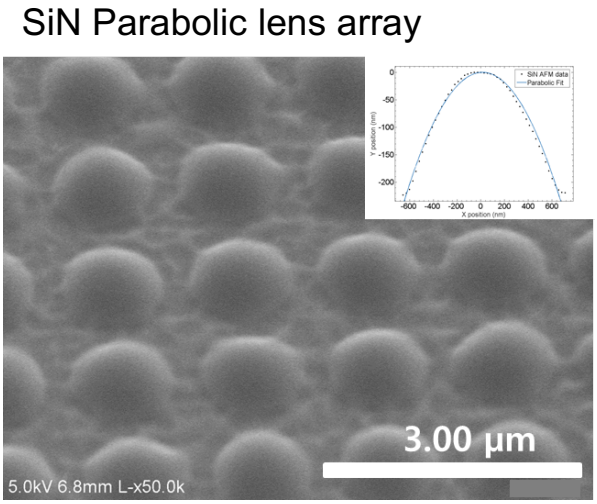

Figure 3.2: SEM image of the nanolenses..

3.3 Design of experiment and results

The simulations indicate that the angular emission pattern should be narrowed (collimated) by adding a lens and that the brightness should thus increase as a result of the increased light collection. For this project, demonstrating the success of the nanolenses could follow two approaches. One could be to demonstrate that the sample demonstrated increased brightness when the lens is added, as compared to the case of no lens. The second approach is to explicitly demonstrate that the nanolenses modify the angular emission pattern from a single nanopillar by measuring in the far field. We take the second approach. While the intensity measurements should indeed be able to demonstrate increased brightness of the lens dots, the dot-to-dot variability in brightness makes this harder to demonstrate when the expected improvements are only on the order of ~2X. However, the characterization of the angular emission pattern generally offers a more information-rich measurement in that we can measure the entire angular emission spectrum rather

than only a single value of the integrated count rate. This choice of approach is borne out by the experimental results which evidence a successful demonstration of the nanolens using these measurements.

To carry out this approach, one question is how to measure the simulated effect of increase light collimation from the nanolens. Typically, imaging the a single nanopillar results only in diffraction-limited spot in the imaging plane. This provides no useful information about the angular spread of the collected light rays. To determine the angular distribution of the emitted light, k-space imaging rather than real-space imaging can be employed. Real space imaging uses an even number of lenses while k-space imaging uses an odd number of lenses. An additional constraint is that the lenses must be pair-wise confocal. The imaging takes place at a plane where angle is mapped into position. One such choice would be the back-focal plane of the first lens. However, in the case of the objective lens, this is actually inside of the optic. Therefore additional lenses must be added (using either 3,5,7 or more lenses).

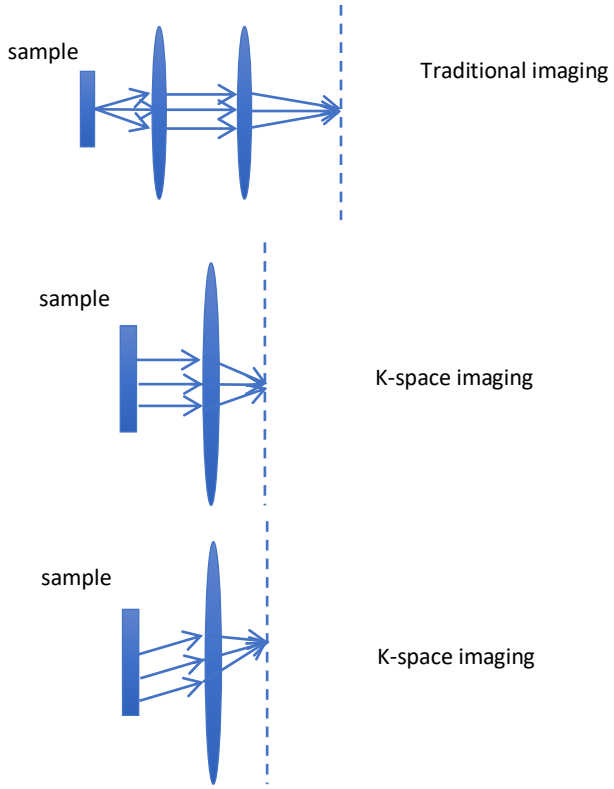

Figure 3.3: Illustration of the k-space imaging concept. Spatial frequency is mapped to a real-space position.

Several experimental requirements needed to be fulfilled in order to complete these measurements. These include the electrical connections, the k-space imaging and the micro-electroluminescence spatial resolution. We describe each of these now.

First, because this was an LED sample it was desired to demonstrate electroluminescence of the sample. This created the requirement of electrical injection. There are two approaches that can be used to electrically inject the sample. The first is to create connections to large sample pads, which can then be wired by hand inside of the cryostat to create connections to the cryostat electrical pin connections. This is then a plug-and-play connection, and the cryostat's electrical connectors may be operated using an SMU (source meter unit). The challenge here is creating the connections to large sample pads, which is typically done using wire-bonds from the tiny contacts

on the sample which measure only ~100um in dimension and are only tens of nm thick. Despite our best attempts to create wire bonds on this sample, we have not had success in this area. Thus, the alternative approach was employed. In this approach, the contact pads on the sample are directly contacted using tungsten probes on micropositioners. Because the probes are located and must be operated outside of a cryostat, this approach is useful for room temperature measurements.

The tungsten probe tips are translated in three dimensions using micrometer screws in order to position the tip onto the contact pad. The shadow of the probe tip may be viewed by imaging the sample. Good contact is generally guaranteed in one of two ways. One, if the sample is only loosely fixed into place, then successfully contacting the probe will gently slide the sample. The second alternative when the sample is rigidly fixed in place is to monitor the current while applying a continuous voltage across the probe, thus when the contact is made a steady current is observed. In our setup, luminescence of different areas of the sample is collected by using fixed collection optics and translating the sample in three dimensions using three motorized micropositioners.

The sample sits on a sample stage which is fixed to the three motorized translation stages. Thus, every time a new part of the sample is to be studied, the sample is moved. In order to avoid the tedious requirement of needing to re-contact the sample after each move, it was desired that the tungsten probe be affixed onto the sample stage. The micropositioners of the tungsten probe were then used to adjust the relative position of the probe on the sample surface. This is shown in the figure below.

The second requirement is to perform the k-space imaging. As described above, this was accomplished using an odd number of pair-wise confocal lenses. In order to accommodate the distance from the sample to the CCD detector on the optical table, approximately two meters of

distance must be covered, and a combination of seven lenses was found to function well for this imaging task. The overall magnification was M = 72 x.

The detector used was a thermoelectrically-cooled CCD in a double grating spectrometer. Because a simple 2D image was desired and not a spectrally-dispersed emission spectrum, the grating was angle tuned to image the undiffracted (reflected) beam from the grating onto the CCD. In this way the CCD imaged the k-space image incident upon the slit of the spectrometer. Ideally,

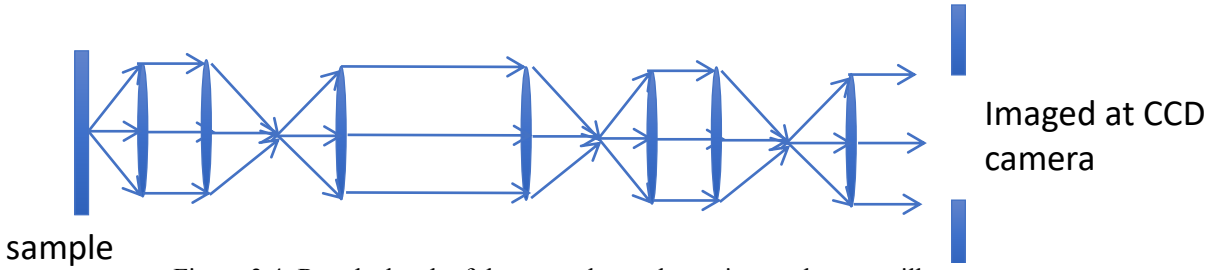

Figure 3.4: Rough sketch of the seven-lens relay to image the nanopillar emission..

the slit width would be wide open, in contrast to the case of spectral measurements where a narrow slit width is required for good spectral resolution.

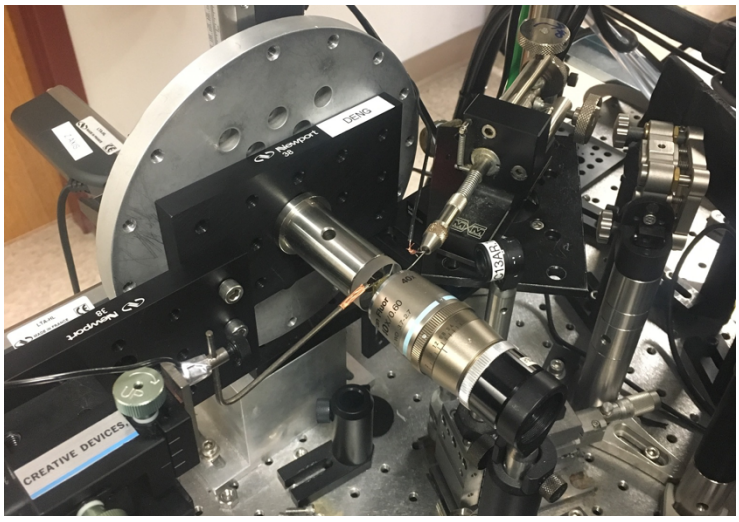

Figure 3.5: Photograph of the micro-electroluminescence setup showing the layout of the sample, n- and p- probe tips on micro-positioners, and objective lens..

The maximum slit width is approximately 3mm, thus the image is cut off by the image of the slit. In the case of our data, the spot size was comparable already to the maximum slit width

and so this constraint did not pose a significant reduction of the image. In future, if greater image width was desired, a number of approaches could be taken. The last lens could be translated over a series of positions and the images could be concatenated in order to achieve a wider spatial range. Alternatively, by sending the beam through a periscope, the x- and y- axes are transformed into one another and thus the image could be stitched together in this manner. For the purposes of these measurements, such measures were not necessary to image with the required spatial range, thus to avoid the complexity of stitching together multiple measurements, a single-image approach was used.

The third requirement is to obtain the required micro-electroluminescence spatial resolution to study single nanopillars. To accomplish the study of single nanopillars, consider a confocal setup with a pinhole of diameter D, placed in an imaging plane with magnification M. The spatial imaging size defined by D/M must be larger than the diffraction limit, which here is

$$d = \frac{\lambda}{2\,NA} \tag{3.3}$$

Here we have $\lambda \sim 500\ nm$ and NA = 0.5, thus the diffraction limit is 500nm. The original pitch of the nanopillars on the fabricated MQW LED sample was only 300nm. Because this resolution exceeds that of the diffraction limit it is not possible to image single nanopillar emission with traditional optics. Therefore, additional metal apertures were added to the sample, designed to limiting the pitch to 4x the original fabrication pitch. With a resulting separation of 1.2um, it was possible to image the neighboring nanopillars. In particular, in the plane of the pinhole, there was a spatial separation of 1.2 um x M, which in our case was equal to 75um, and using a 50um pinhole we are able to image only a single nanopillar at a time. An additional complication is that it was believed the fabricated apertures did not work perfectly, thus there could be multiple

nanopillars emitting light beneath each nanolens. The effect of this complication is manifest in the measurements and explains some of the observed features as we will describe.

We collected images using 60 second exposures in order to obtain good signal to noise. Such long exposures are necessary because the light is being dispersed onto a large number of pixels on the CCD array. The total CCD array consists of 1024 x 256 pixels along x and y respectively, with pixel widths of 25um. The slit limits the horizontal extent of the image to some ~3mm = 120 pixels, while the full vertical range of 256 pixels is maintained. In typical PL measurements, the light is incident at zero wavelength onto a single pixel and for the diffracted beam is dispersed across the horizontal axis. Thus this measurement represents a reduction of signal strength per pixel of ~256x compared to the typical PL measurement. Compensating for this reduction in signal strength we therefore increase the exposure time. The high quantum efficiency

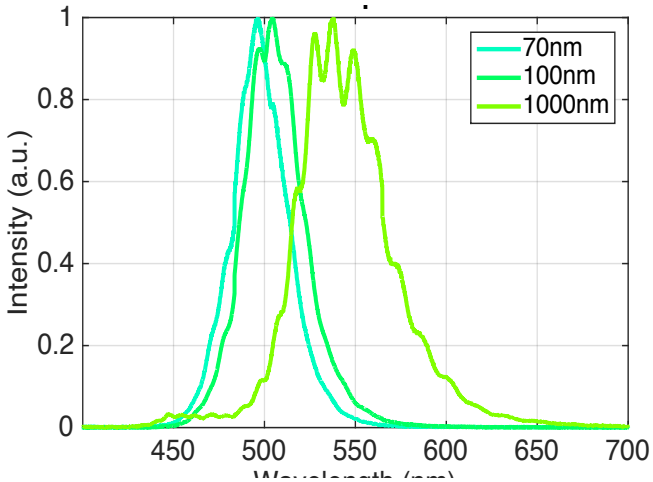

Figure 3.6: Measured micro-electroluminescence spectra showing the emission pattern for varying nanopillar diameter. The fringes are Fabry-Perot type interference from reflections in the sample..

of the CCD also facilities this measurement. With such long exposure times and because the slit must be left open, any stray light will cause an appreciable signal. The use of basic light blocking

measures using black carboard to reduce stray light outside of the main beam path is therefore essential in this experiment.

The results of the measured spectra are shown in Fig. 3.6. With 8V applied voltage, the current was approximately 100uA and was current-limited using a source-meter-unit to avoid damage to the sample. We observe a broad EL signal which also contains oscillations. These are often observed in EL from LED samples and we believe they are due to Fabry-Perot-type oscillations arising from interference effects from reflections within the sample, to which this effect is commonly attributed. We see these oscillations are reduced with the lens in Fig. 3.7.

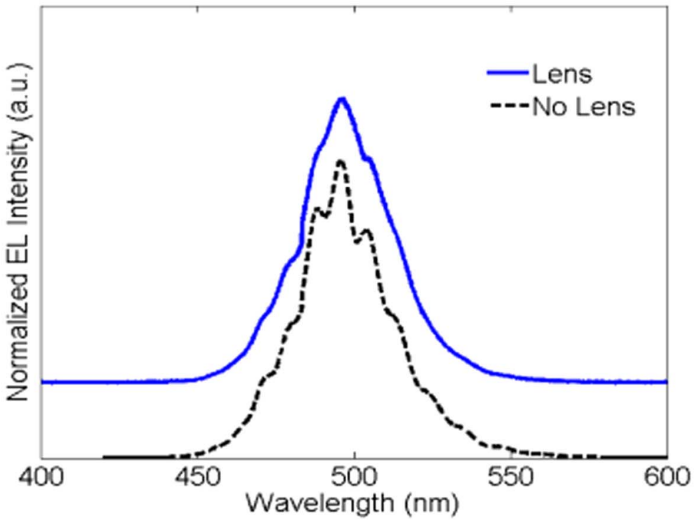

Figure 3.7: Comparison of lens and no-lens EL measurements. The interference fringes seem to be reduced by the lens, indicating a reduction of internal reflections. The effect of the lens result is further investigated using k-space imaging.

The k-space images for a sample lens and no-lens nanopillars with a diameter of 70nm are shown in Fig. 3.8. The simulated prediction is shown in Fig. 3.9. There is significant variation from nanopillar to nanopillar. Nonetheless there does appear to be a trend demonstrating an

enhancement in light collimation by 1.9x for the lens nanopillars. This result is plotted in line plots which integrate across the images, as shown in Figure 3.10.

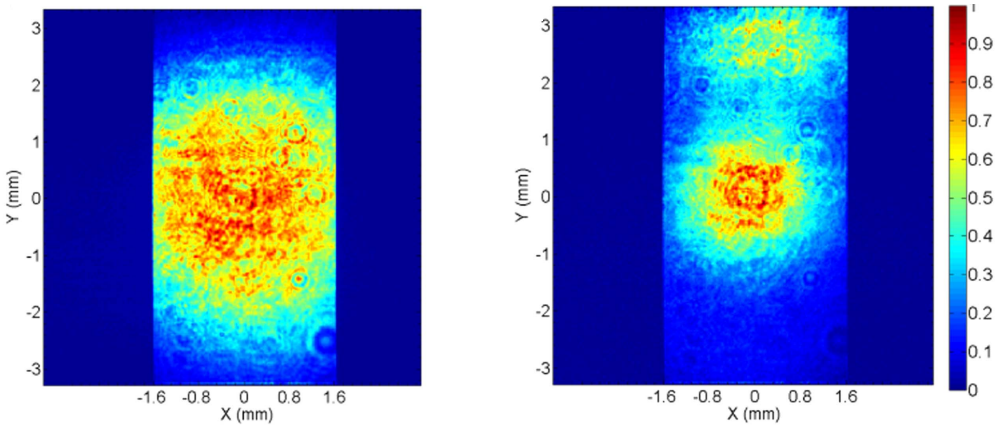

Figure 3.8: Measured k-space images on the CCD, showing the reduction in the spread of the angular emission pattern with the nanolens. The left image is a bare nanopillar, the right image is a nanopillar with the nanolens..

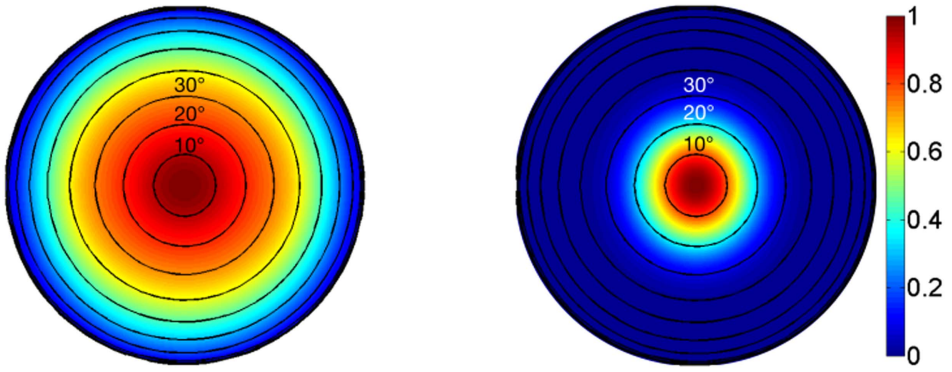

Figure 3.9: Simulated far field image pattern from a single nanopillar, predicting a reduction in the FWHM of the angular emission pattern by a factor of 2.8x using the nanolens. The left is a bare nanopillar, the right is a nanopillar with a nanolens.

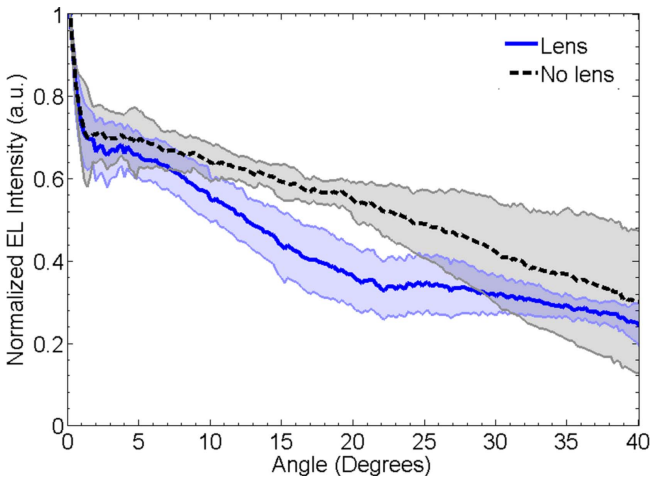

Figure 3.10: Angular emission pattern obtained from fitting the 2D images with annular discs and averaging across seven nanopillars of each type.

3.4 Summary

In this chapter we have described micro-electroluminescence measurements and k-space micro-electroluminescence of blue and green emitting InGaN/GaN nanopillars to show the enhancement of light collimation using integrated nanolenses on single nanopillars. We demonstrate a reduction in the average angular spread of 1.9x for the nanopillars with lenses as compared to the bare nanopillars. This is comparable to the 2.8x enhancement predicted by simulations of the structures. This result supports the usefulness of InGaN nanopillars for micro-display technologies. The nanolens concept provides a successful demonstration of how nanopillars may be integrated with additional fabricated nanostructures to enhance device performance for particular applications.

Chapter 4
Plasmonic enhancement of InGaN/GaN QDs

In this chapter, we describe measurements of top-down etched InGaN/GaN quantum disks in nanopillars with enhanced brightness and radiative emission rate using an open-top plasmonic cavity. In section 4.1, we introduce the motivation of making faster and brighter single photon sources and the related physics. In section 4.2, we describe the sample and details of its structure and fabrication. In section 4.3 we present the measurements which demonstrate the enhanced brightness and radiative emission rate of the open-top cavity as compared to a closed-top cavity and to a control sample. Section 4.4 offers a conclusion.

4.1 Motivation

The radiative recombination rate of a single photon emitter is important in several ways for applications in quantum technology. First, obviously faster emission rates are useful for increasing the bit rate for sending information. Second, faster emission also generally increases the quantum efficiency because of the competition between radiative and nonradiative recombination. Third, applications such as two-photon interference in quantum computation require indistinguishable photons. Indistinguishability cannot be achieved unless the spontaneous emission rate exceeds the pure dephasing rate. Thus, reducing the decoherence mechanisms is often a major effort in developing candidate systems for quantum technology, and this effort is complemented by efforts to enhance the radiative lifetime, which is the approach demonstrated here.

The spontaneous emission rate from a two-level system is proportional to the density of states (DOS). This offers a way to increase the emission rate of a two-level system by enhancing the DOS. The enhancement of the DOS is related to the Purcell factor, which is proportional to the ratio Q/V where Q is the quality factor and V is the mode volume.

A variety of different types of cavity systems have been used to enhance the spontaneous emission rate in different systems. However, some cavity designs such as photonic crystals are difficulty to integrate with quantum dots because they are highly dependent on the position and the emission wavelength of the individual QDs. In the case of our site-controlled QDs, the positioning is not a major problem, however the QDs in our samples do suffer from inhomogeneous broadening and so a photonic crystal would typically have too narrow of a resonance to ensure good coupling with each QD. Instead, in this study we use a plasmonic cavity, which is based upon coupling the QD to a surface plasmon of a metal coating.

4.2 Sample fabrication

The InGaN/GaN QDs used in these studies were fabricated by the group of PC Ku in EECS at UM. Their fabrication begins with a commercially available InGaN/GaN single quantum well wafer. The QW is grown on a c-plane sapphire substrate by metal-organic chemical vapor

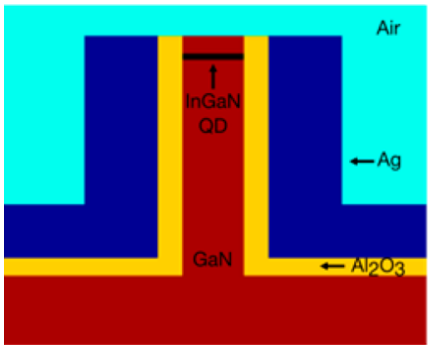

Figure 4.1: Schematic of the open-top cavity design.

deposition (MOCVD). Electron beam lithography is used to pattern the sample. The etching process to implement the design is accomplished using both reactive ion etching and wet etching.

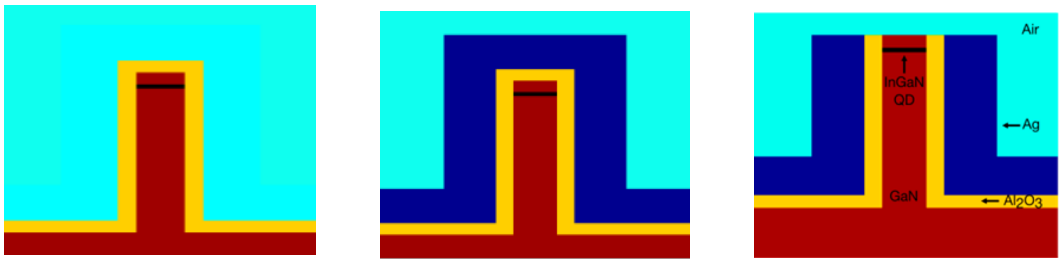

Figure 4.2: Comparison of the open-top cavity design with that of the closed-top cavity and the control sample.

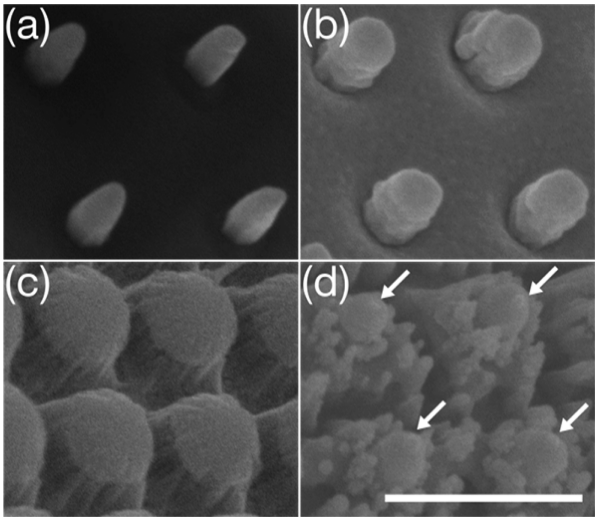

Figure 4.3: SEM images showing fabrication of the open top cavity; the scalebar is 300 nm. (a) Bare nanopillars. (b) After aluminum oxide and silver deposition. (c) After planarization with SiO_2 and etchback. (d) After removal of SiO_2 and silver. Exposed nanopillars indicated by arrows.

To achieve significant plasmonic enhancement, the extinction band of the surface plasmon must be wavelength matched to the desired emission wavelength [38]. A number of variables of the nanoscale metallic particles must be tuned, including material, size, shape and spacing. In our case, the samples are coated in silver because the plasmonic resonances of thin silver cavities matches the emission energy of our InGaN disks. The thickness of the coating must be tuned to match the emission energy. In our case a 30nm thick Ag coating was applied. The spacing between the silver and the InGaN emitter must also be optimized in order to achieve good coupling between the exciton and the surface plasmon. For this purpose, a 2nm SiO2 spacer layer is applied between the nanopillar and the silver coating. A control sample was also fabricated which consisted of an Aluminum coating rather than silver. Because the surface plasmon resonance of aluminum is not well matched to the InGaN emission energy, no plasmonic enhancement is expected in this case. The reason for the use of an open top cavity as opposed to the closed top is mostly to improve the light extraction from the structure. The open top cavity is shown in Fig. 4.1 and contrasted with the other two samples in Fig. 4.2. SEM images of the fabrication are shown in Fig. 4.3.

4.3 Measurements and analysis

Because the cavity enhances the local electric field experienced by the carriers in InGaN, the control and cavity samples would experience different local electric fields and thus different piezoelectric screening. This would tend to cause an increase in the radiative emission rate due to the quantum confined stark effect. Although this does result in an enhancement of the silver coated

structure, it is separate from the plasmonic enhancement under study. Thus, in order to separate out these effects, maximal piezoelectric field screening is achieved by exciting the samples at high power where saturation should be reached. This is typically around 10mW of power. This is shown in Fig. 4.4.

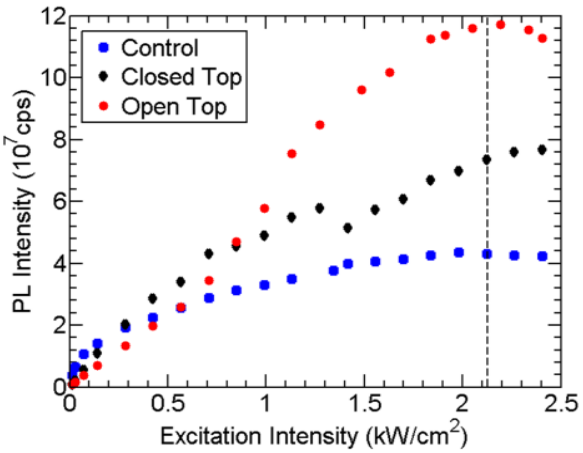

Figure 4.4: Measured power-dependent PL in order to determine saturation for the samples.

The PL and TRPL measurements are shown in the figures 4.5 and 4.6. This study demonstrated enhancement using measurements of ensembles of QDs. The open top cavity proved to be 2.4x brighter and 2.6x faster than the control sample.

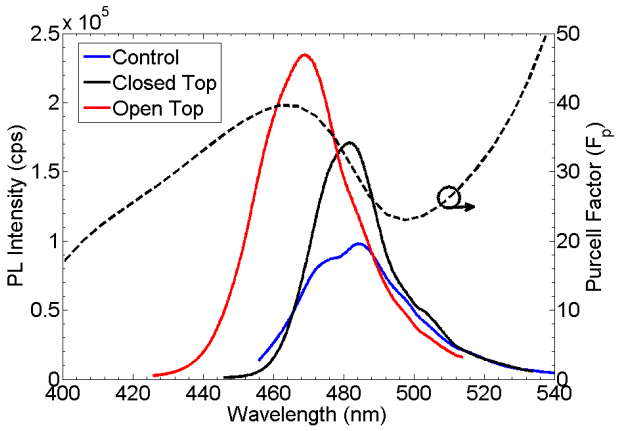

Figure 4.5: Measured PL spectra showing the enhanced brightness of the open top cavity QDs.

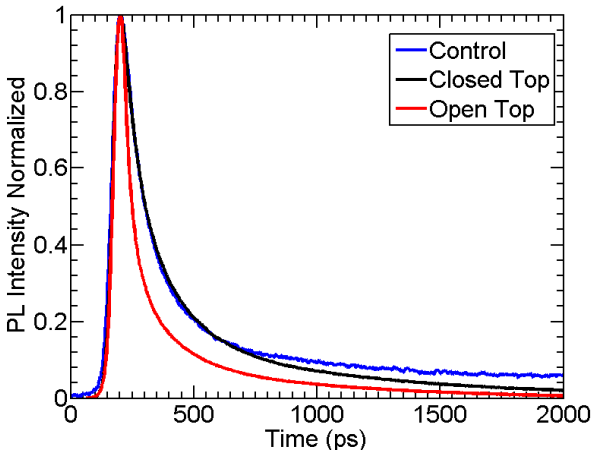

Figure 4.6: Time resolved PL demonstrating the reduced measured lifetime in the open-top cavity sample.

4.4 Conclusions

In this chapter, we presented optical measurements demonstrating an open-top plasmonic cavity on nanopillars containing a single InGaN quantum disk. Intensity measurements in PL and lifetime measurements from time resolved PL were used to characterize the sample and compare the results from the open-top cavity with that of a closed-top cavity and a control sample. The open-top cavity showed enhanced brightness and recombination rate. While the measured cavity enhancement is much less than the theoretical prediction, it is believed this may be due in part to the use of aluminum doped silver rather than pure silver in the coating of the nanopillars. This was utilized in order to provide smoother deposition onto the surface of the nanopillars. In future, developments in the fabrication could result in the ability to deposit smooth surfaces using more pure silver. Additionally, future work could include the development of more complex, multi-layer cavity structures to further enhance the Purcell factor of these structures.

Chapter 5
Effect of strain asymmetry on exciton-phonon interaction in elliptical InGaN quantum dots

In this chapter we examine the exciton-phonon interaction in elliptical QDs. In section 5.1 we describe the motivation of studying the exciton-phonon interaction and the role of asymmetrical strain in an elliptical QD. Section 5.2 describes polarization-resolved micro photoluminescence measurements of single quantum disks which demonstrate a high degree of linear polarization (DOP) along the direction of the long axis of the quantum disk ellipse, due to the strain engineering of the elliptical disks. In section 5.3 we investigate the effect of strain asymmetry on the polarization properties of the first optical phonon replica, and theoretically predict the difference in phonon coupling strength of the hole envelope functions corresponding to x- and y- polarized emission. In section 5.4 we derive the expected effect of this variation of phonon coupling on the degree of polarization of the phonon replica. Additionally we present the experimental data to compare to this prediction. Section 5.5 summarizes these results.

5.1 Motivation of studying the exciton-phonon interaction and the role of asymmetrical strain in an elliptical QD.

The study of exciton-phonon interaction in nitride nanostructures is an important area for understanding and improving nitride-based materials for device performance. For instance, it is believed that Auger recombination, in which the energy of the electron and hole are transferred to a third charge carrier rather than generating a photon, plays an important role in limiting the

efficiency of LEDs. In indirect Auger, the scattering process is assisted by a phonon. This is a nonradiative recombination mechanism, contributing to the efficiency droop and green gap issues which are major areas of needed development in nitride LEDs. Exciton-phonon interactions are also responsible for line broadening and decoherence mechanisms which are fundamental to the performance of classical and quantum devices.

In this work we focus on the phonon interaction relating to the longitudinal optical (LO) phonon replica, which is commonly observed in the photoluminescence spectra of InGaN and its nanostructures. These emission peaks are redshifted from the main zero-phonon line (ZPL) by the energy of an LO phonon, approximately 91meV in GaN, corresponding to emission of a photon accompanied by creation of a phonon. The strength of the exciton-LO phonon interaction is given by the Huang-Rhys factor S. In particular, we have [39]:

$$S = \frac{{f_0}^2}{(2\pi)^3(\hbar\omega_{LO})^2}\int \frac{1}{|\boldsymbol{k}|^2}|\mathcal{F}(|\psi_e|^2 - |\psi_h|^2)|^2\, d^3\boldsymbol{k} \tag{5.1}$$

$$f_0^2 = 2\pi e^2 \hbar\omega_{LO}\left(\frac{1}{\epsilon_\infty} - \frac{1}{\epsilon_0}\right) \tag{5.2}$$

As shown in Eqn. 5.1 above, S depends on the charge density (the difference in probability densities of the electron and hole), and thus modifying the electron and hole wavefunctions due to strain will have an effect on S.

The Huang-Rhys factor defines a series of phonon replicas with intensities given by [39]:

$$I_n = I_0 \frac{S^n e^{-S}}{n!} \tag{5.3}$$

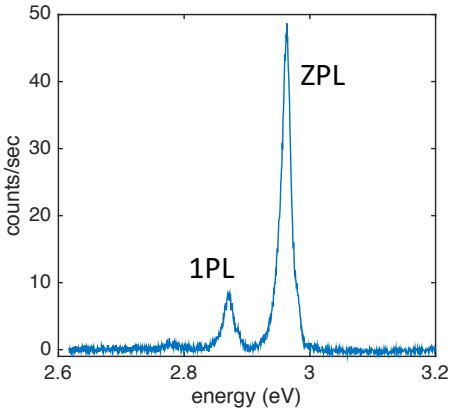

Figure 5.1: PL of a single 22nm x 36nm QD showing the zero phonon line (ZPL) and first optical phonon line (1PL).

A PL spectrum of a single QD showing this intensity distribution is shown in Fig. 5.1.

In this case, in order to study the effect of strain on exciton-phonon coupling, we utilize the strain engineering that arises from controlling the shape of elliptical quantum dots. In fact, by introducing asymmetry in the structure of individual QDs with an elliptical shape, polarized single photon sources have been demonstrated with a high degree of linear polarization in nitride QDs. The application of such efforts is for quantum technology as described in Chapter 1. In particular, the most popular quantum cryptography protocols utilize the polarization degree of freedom encode information onto single photon states. Thus, it is desirable to have a deterministic source of polarized single photons. To directly implement a protocol such as BB84, it would be desirable to generate photon with polarizations in eigenstates of the horizonal/vertical and diagonal/anti-diagonal bases. As we describe next, top-down etched elliptical QDs offer a means to generate polarized photons with a high degree of polarized and with polarization parallel to the fabricated orientation of the long axis of the ellipse.

5.2 Polarized single photon emission with high DOP from elliptical QDs

The elliptical QDs used in this study were fabricated from a 3-nm thick InGaN/GaN quantum well sample grown using MOCVD on a sapphire substrate. The position, size, orientation

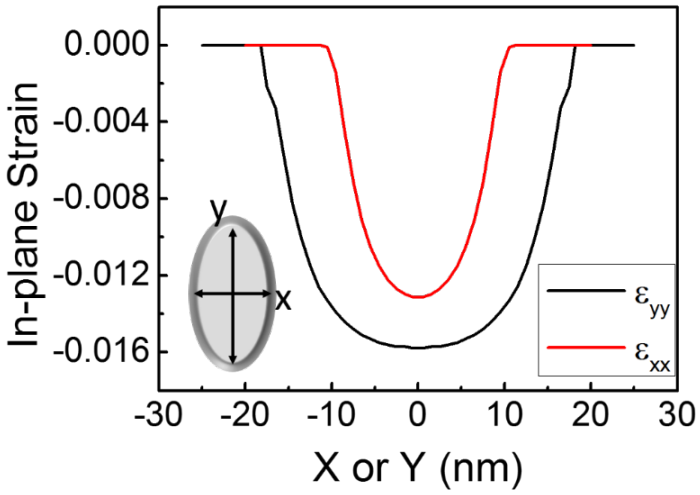

Figure 5.2: Strain asymmetry in an elliptical QD. Image from [40].

and aspect ratio of the elliptical QDs this study were fabricated using electron beam lithography and using plasma and chemical etching [40]. The elliptical QDs fabricated with dimensions of 22nm x 36nm - specifying the long and short axis of the ellipse, respectively - were chosen for this study. Elliptical QDs have an asymmetric strain, which results in eigenstates polarized parallel to the long and short axes of the ellipse. The oscillator strength of the eigenstates polarized along the long axis is greatly enhanced relative to that of the short axis, leading to a large degree-of-linear-polarization (DOP).

To describe the degree of polarization, the hole wavefunction can be factored as [40]

$$\Psi_h = \varphi_{h,x} \cdot \mathrm{X} + \varphi_{h,y} \cdot \mathrm{Y} + \varphi_{h,z} \cdot \mathrm{Z} \qquad (5.4)$$

where X, Y, and Z are the Bloch basis functions and the envelope functions are $\varphi_{h,x}$, $\varphi_{h,y}$, $\varphi_{h,z}$. Meanwhile the electron wavefunction is composed of the S-type wavefunction:

$$\Psi_e = \varphi_e \cdot \mathrm{S} \tag{5.5}$$

With this factorization, the transition matrix elements corresponding to x polarized emission and y polarized emission are:

$$|M_x|^2 = |\langle \Psi_e | p_x | \Psi_h \rangle|^2 \cong |\langle \mathrm{S} | p_x | X \rangle|^2 \left| \langle \varphi_e | \varphi_{h,x} \rangle \right|^2 \tag{5.6}$$

$$\left|M_y\right|^2 = \left|\langle \Psi_e | p_y | \Psi_h \rangle\right|^2 \cong \left|\langle \mathrm{S} | p_y | Y \rangle\right|^2 \left| \langle \varphi_e | \varphi_{h,y} \rangle \right|^2 \tag{5.7}$$

This gives a degree of linear polarization (DOP):

$$\mathrm{DOP} = \frac{\left|M_y\right|^2 - |M_x|^2}{\left|M_y\right|^2 + |M_x|^2} \tag{5.8}$$

Experimentally, DOP is calculated as:

$$DOP = \frac{I_y - I_x}{I_y + I_x} \tag{5.9}$$

In order to measure these effects experimentally, a microphotoluminescence setup was used to measure the light emission from single QDs. The QDs were excited using non-resonant laser excitation with energy below the GaN bandgap. The measurements were carried out at 10K. The polarization resolved photoluminescence spectra of the QD emission was collected by rotating half-wave plate which was followed by a linear polarizer, after which the light was routed to the spectrometer and dispersed onto a thermoelectrically cooled CCD.

The degree of polarization of the main emission line was modeled using nextNano simulations including strain to calculate the wavefunctions corresponding to x- and y- polarized emission. It was found that a degree of polarization of approximately 0.91 was predicted. A few

of the dots indeed showed a high DOP with values comparable to the predicted value. As predicted, the measured polarization was aligned with the long axis of the ellipse. For the remaining dots, the measured DOP values are slightly reduced from the theoretical prediction, with typical values of 0.79. The reduction in DOP is believed to be mainly due to irregularities in the fabricated shape and size of the QDs, as indicated by comparisons of the measured DOP to the SEM images of individual QDs [40] .

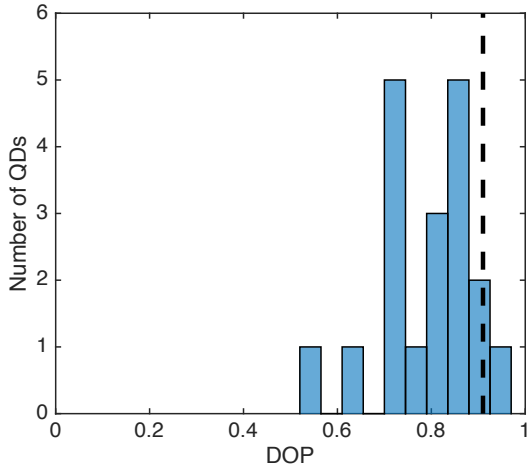

Figure 5.3: Histogram of degree of polarization (DOP) of zero-phonon line of nineteen QDs of size 22nm x 36nm. The vertical dashed line indicates the theoretical prediction of DOP = 0.91.

5.3 Effect of strain on phonon coupling strength

Because the strain affects the electron and hole wavefunctions and thus affects the Huang-Rhys factor S, the control of strain in elliptical QDs should be a means of studying the exciton-phonon coupling. In order to carry out this study, we calculate the electron and hole wavefunctions in the basis described in the previous section. We have completed this calculation using nextNano models of the nanostructures to determine the wavefunctions. In Fig. 5.4, we see the envelope function of the electron ground state. Because the lateral strain profile generates the preferential

emission along the long axis (y) of the ellipse, the differently polarized eigenfunctions of the hole will have spatial dependence that is influenced by the lateral strain profile. Indeed, in Fig. 5.5 we see that $\varphi_{h,x}$ is more concentrated along x = 0 (where x strain is greatest) while $\varphi_{h,y}$ is more concentrated along y = 0 (where y strain is greatest).

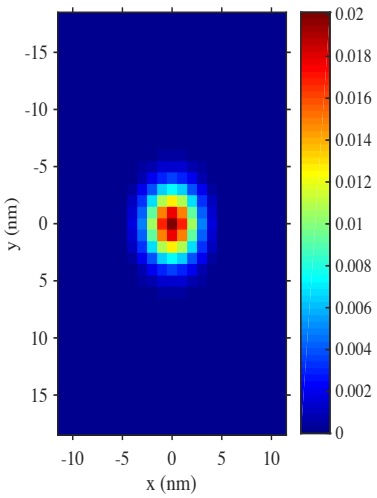

Figure 5.4: The probability density ΨΨ* of the electron ground state for a constant z-value.

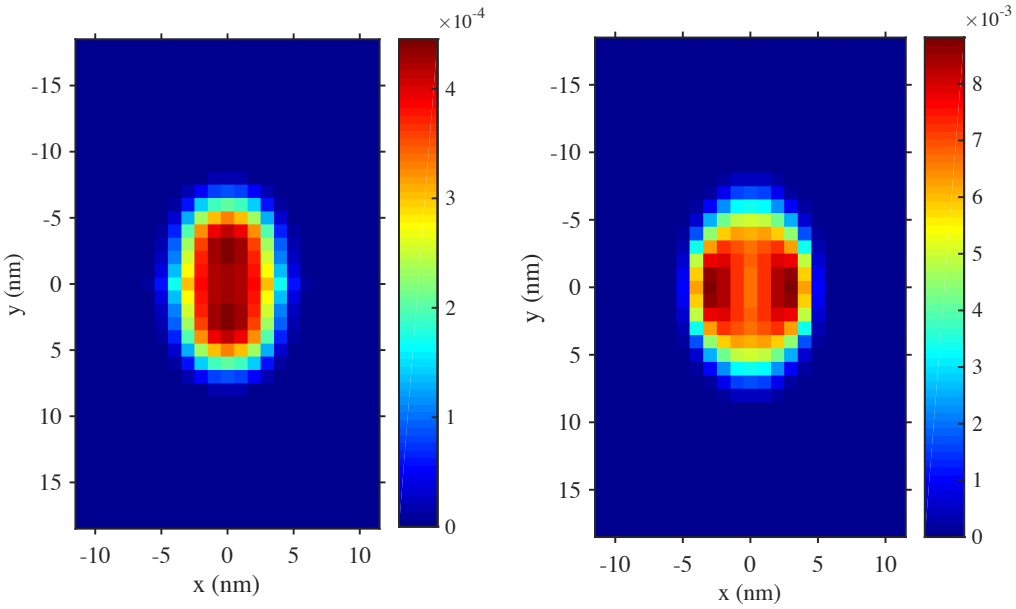

Figure 5.5: (a) The probability density corresponding to the hole ground state envelope function responsible for x-polarized emission. (b) Likewise for y-polarized emission. Note that the scale of the values is much greater for the y-polarized emission, as this is the dominant polarization direction of the total wavefunction.

Applying these wavefunctions to calculate the S values using Eqn. 6, we proceed to take Fourier transforms of the difference of the probability density functions of the electron and hole for each of the hole wavefunctions. Due to its reduced overlap with the electron wavefunction, the x-polarized wavefunction has somewhat larger values of the relevant quantity in frequency space (namely the charge density). In particular, we find $\frac{S_x}{S_y} = 1.080$. As we describe in the next section, the degree of polarization of the optical phonon replica offers a means to observe the predicted change in phonon coupling strength that arises from the strain asymmetry.

5.4 Degree of polarization of optical phonon replica

We now derive simple expressions for the degree of polarization of the zero phonon line and of the first phonon replica, DOP_{ZPL} and DOP_{1PL}. Our result shows the intuitive result that

measurements of these values provides a way to quantify the different coupling of phonon to the two cross polarized states $\varphi_{h,x}$, $\varphi_{h,y}$ which was predicted in the previous section.

Considering the zero phonon line and the first phonon replica, and examining the two states $\varphi_{h,y}$ and $\varphi_{h,x}$ with generally different Huang-Rhys couplings S_x and S_y, we have:

$$I_{y,1PL} = S_y I_{y,ZPL} \tag{5.10}$$

$$I_{x,1PL} = S_x I_{x,ZPL} \tag{5.11}$$

Substituting $\varphi_{h,y}$ or $\varphi_{h,x}$ for ψ_h in Eqn. 5.1 obtains S_y and S_x. To understand quantitatively the effect of these values on the relative DOP of the 1PL compared to DOP of ZPL, we explicitly define the DOP of the zero-phonon line (ZPL) and the one-phonon line (1PL) are:

$$DOP_{ZPL} = \frac{I_{y,ZPL} - I_{x,ZPL}}{I_{y,ZPL} + I_{x,ZPL}} \tag{5.12}$$

$$DOP_{1PL} = \frac{I_{y,1PL} - I_{x,1PL}}{I_{y,1PL} + I_{x,1PL}} \tag{5.13}$$

Solving we find:

$$\frac{S_x}{S_y} = \frac{(1 + DOP_{ZPL})(1 - DOP_{1PL})}{(1 - DOP_{ZPL})(1 + DOP_{1PL})} \tag{5.14}$$

This result indicates that for $S_x > S_y$, there is a reduction in the DOP_{1PL} compared to DOP_{ZPL}. This is because the cross polarized eigenstates $\varphi_{h,x}$ has a stronger phonon coupling (according to the theoretical prediction) and thus contributes more significantly to the phonon replica, reducing the DOP of the phonon replica. To test this prediction, we plot the measured DOP_{1PL} compared to measured DOP_{ZPL} for nineteen individual 22nm x 36 nm elliptical QDs. The results are shown in Fig. 5.6.

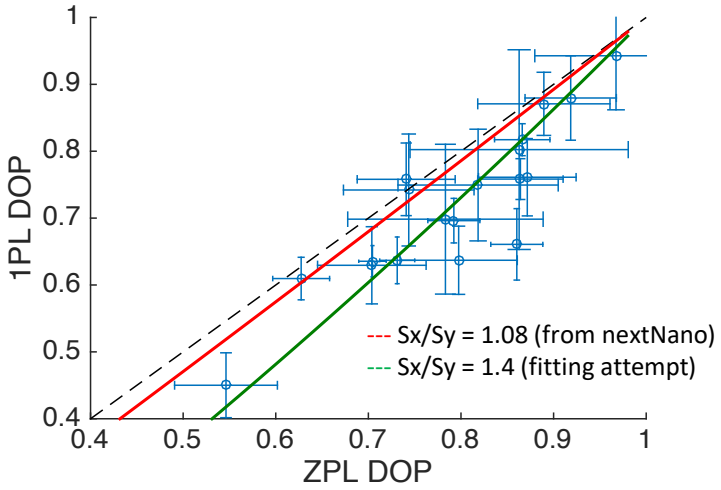

Figure 5.6: Experimental DOP data and fits using two different constant values of the ratio S_x/S_y. The dotted line is x = y. The red curve uses $S_x/S_y = 1.08$, the theoretical result, and seems to be consistent with high DOP dots. The green curve uses the value $S_x/S_y = 1.4$ and is a fitting attempt for lower DOP dots.

In agreement with the theoretical prediction, we see that indeed the degree of polarization is reduced as compared to the ZPL. The error bars arise from the fitting uncertainties of the nonlinear fitting used to obtain the DOP from the polarization-resolved PL measurements. Nearly all the points lies below the line y = x, indicating that there is indeed a statistically significant reduction of the DOP of the phonon replica as compared to that of the ZPL. We also see that the

DOP of the phonon replica is correlated with the DOP of the ZPL. To examine this correlation, we attempt a fit using Eqn. 5.14.

Two fitting curves to the data (which are defined by Eqn. 5.14) are shown for reference on the figure. The value $\frac{S_x}{S_y} = 1.08$ corresponds to the theoretically predicted curve. This should apply reasonably well to the QDs whose measured DOP agree well with the theoretical prediction, namely $DOP_{ZPL} = 0.91$. Indeed, we see a reasonable agreement of the fitting curve for the few highest DOP QDs. Thus, the results from the highest DOP QDs seem to be consistent with theoretical predictions. However, we also note that for these highest DOP QDs, the ZPL and 1PL are expected to have similar DOP except for values of $\frac{S_x}{S_y}$ which deviate significantly from unity. Thus, while the measured results for the high DOP QDs are consistent with our theoretical predictions of the effect of strain on phonon coupling strength, in fact it is the lower DOP QDs which are more sensitive to variations in $\frac{S_x}{S_y}$.

As mentioned previously, lower DOP QDs are believed to arise from irregularities in the QD shape and size which results in discrepancy from the theoretically predicted DOP, as was confirmed using SEM images of a few QDs to correlate shape with measured DOP [40]. For these QDs, as the measured DOP is significantly less than the theoretically predicted value, the theoretically calculated wavefunctions are not believed to provide accurate predictions of the DOP or of the phonon coupling strength. As a preliminary attempt to fit these data points (which constitute most of the data), we also include in the figure a fitting curve using $\frac{S_x}{S_y} = 1.4$, which seems to provide a reasonable fit. This motivates the further study of these QDs, and of QDs with lower aspect ratio which have a theoretically predicted lower DOP.

5.5 Summary

This work investigated the mechanism by which the phonon coupling strength is affected by asymmetrical strain in elliptical QDs. In particular, we examined the LO phonon replica in the PL of nineteen single QDs with designed dimensions of 22nm x 36 nm. NextNano calculations of the ground state wavefunctions suggest that for our 22nm x 36nm QDs, the phonon coupling of the envelope function corresponding to the orthogonal polarization (x) is enhanced by approximately 8% compared to that of the dominantly polarized hole envelope function (y); that is, $\frac{S_x}{S_y} = 1.08$.

In order to test these predictions, we derived an intuitive description of the effect of this asymmetrical phonon coupling on the degree of polarization of the phonon replica. Because the hole envelope function associated with the dominant y-polarization has reduced phonon coupling compared to hole envelope function associated with x-polarization, we expect a reduction in the DOP of the phonon replica. Indeed, we observe that nearly all of the QDs show a reduction in the DOP of the phonon replica compared to that of the ZPL. The experimental results thus seem to support the theoretical prediction of a reduced DOP of the phonon replica.

To fit the observed data points, the theoretical predictions should only be expected to be accurate for QDs for which the DOP of the zero phonon line agrees reasonably with the theoretical prediction, which is $DOP_{ZPL} = 0.91$. Lower DOP QDs are believed to arise from irregularities in the QD shape and size which results in discrepancy from the theoretically predicted DOP. Indeed, we see a reasonable agreement of the fitting curve using $\frac{S_x}{S_y} = 1.08$ for the few highest DOP QDs. Thus, the results from the highest DOP QDs seem to be consistent with theoretical predictions. However, in fact the lower DOP QDs are more sensitive to variations in $\frac{S_x}{S_y}$.

The lower DOP dots seem to fit reasonable with the fitting curve using $\frac{S_x}{S_y} = 1.4$. This motivates the further study of these QDs, and of QDs with lower aspect ratio which have a theoretically predicted lower DOP. More generally, these results also motivate further studies into using the sort of top-down etched fabrication method applied to create our elliptical QDs as a tool which could be used to control the exciton-phonon interaction in nanostructures; as we have seen, the ground state wavefunctions and their coupling to the phonon are influenced by the strain profile that is generated by the geometry of the fabricated structure.

Furthermore, while our simulation did not include localization effects such as indium composition fluctuation, recent work in the field has included localization in the simulations in order to accurately model the electron and hole wavefunctions [16], and this would be a useful area to pursue to address topics such as that describes in this chapter.

Chapter 6
Effect of nanopillar diameter on exciton-phonon coupling

In this study, we examine the coupling strength of the exciton to the LO phonon in photoluminescence of etched InGaN/GaN quantum disks of diameters ranging from 60nm to 1um as well as the unetched quantum well. In section 6.1, we introduce the concept of using the phonon coupling strength to determine the localization length and describe previous findings on this topic. In section 6.2, we describe measurements of PL of etched InGaN/GaN quantum disks. In section 6.3, we model the exciton wavefunction and extract the localization length from the phonon coupling strength. In section 6.4, we offer a conclusion.

6.1 Phonon coupling strength and previous findings

As previously mentioned, the study of exciton-phonon interaction in nitride nanostructures is an important area for understanding and improving nitride-based materials for device performance. The coupling strength in the case of the optical phonon replica in the PL is quantified using the Huang-Rhys factor S which measures the relative strength of phonon replicas, as described in the previous chapter.

The S factor is sensitive to strain in that strain affects the wavefunctions in InGaN, most notably due to the piezoelectric fields which separate the electron and hole along the growth direction of a quantum well (QW). Previous studies in InGaN quantum wells have typically found a negative correlation of emission energy with the relative emission strength of the phonon replica.

The origin of this trend typically arises from an increase in strain, which causing both a reduced emission energy and enhancement of the optical phonon interaction due to the influence of strain on the electron and hole wavefunctions. The effect of strain has been studied in this manner by examining different samples of varying well thickness or indium concentration [11], [41] [42] [43], [44]. In these studies, the increase in the piezoelectric fields due to either thicker QWs or higher indium concentration resulted in an increase in the Huang-Rhys factor. This arises because the larger vertical separation of the electron and hole results in a larger charge density and greater coupling to the phonon.

6.2 Photoluminescence of InGaN/GaN quantum disks

In this study the strain is tuned by fabrication control of the nanopillar diameter, with well thickness or indium concentration held constant, and the effect of diameter on phonon coupling strength is examined. The QDs used in this study were fabricated from a 3-nm thick InGaN/GaN quantum well sample grown using MOCVD on a sapphire substrate. The device was fabricated by Chu-Hsiang Teng in the group of Professor PC Ku at UM-EECS. The position and size of the QDs in this study were fabricated using electron beam lithography and using plasma and chemical etching, as has been described previously [40]. The QDs studied here were fabricated with diameters ranging from 60nm to 1um. For each diameter, the sample contained an array of nanopillars with an area of 100um x 100um and with a nanopillar pitch which varied from 300nm for the smaller diameters up to several um for the larger diameter. Arrays consisting of QDs of the same diameter were excited using non-resonant laser excitation with energy below the GaN bandgap. The measurements were carried out at 10K. The light was routed to the spectrometer and dispersed onto a thermoelectrically cooled CCD.

The lateral potential profile allows for a great deal of control over the emission energy for the etched nanopillars as we now describe. Due to strain relaxation at the edges of the nanopillars, the piezoelectric fields are reduced in nanopillars. This strain relaxation thus allows the emission energies of quantum wells to be gradually tuned by controlling the diameter of the nanopillar through plasma etching and chemical etching. This effect has been demonstrated as a means of tuning the emission of InGaN nanopillars across most of the visible spectrum even with fixed indium concentration. The lateral strain profile and the resulting lateral potential profile have been effectively modeled in these systems. A simple model of the radial potential given by:

$$\phi(r) = -B_m[1 - \operatorname{sech}\left(\frac{\kappa D}{2}\right)\cosh(\kappa r)] \quad (6.1)$$

Here κ represents a strain relaxation length in the nanopillar, as strain is relaxed at the sidewall, with more strain towards the center of the nanopillar. B_m represents the energy redshift due to strain in a QW.

Due to strain relaxation at the edges of the nanopillars, the piezoelectric fields are reduced in nanopillars. This strain relaxation thus allows the emission energies of quantum wells to be gradually tuned by controlling the diameter of the nanopillar through plasma etching and chemical etching. This effect has been demonstrated as a means of tuning the emission of InGaN nanopillars across most of the visible spectrum even with fixed indium concentration. The lateral strain profile and the resulting lateral potential profile have been effectively modeled in these systems. By assuming that the excitons relax to the potential minima at the center of the nanopillar (r=0), the emission energy of InGaN disks in nanopillars as a function of nanopillar diameter is thus given by:

$$E(D) = E_0 - B_m\left[1 - \operatorname{sech}\left(\frac{\kappa D}{2}\right)\right] \quad (6.2)$$

This model has been well supported by the data of emission energy vs diameter for nanopillar samples across a range of diameters. These results indicate a good understanding of the variation of piezoelectric field strength as a function of diameter in this system.

Fig. 6.1 shows a characteristic PL measurements for the D=600nm nanopillars. In total thirteen different arrays were measured of diameters ranging from 1um to 60nm. The PL in each case consists of a relatively broad Gaussian with a distinct phonon replica. The smallest diameter nanopillars in fact show an enhancement of S relative to the larger diameter etched nanopillars. Although there are fluctuations, this trend is clearly observed in Fig. 6.2 which shows the results for all thirteen QD arrays.

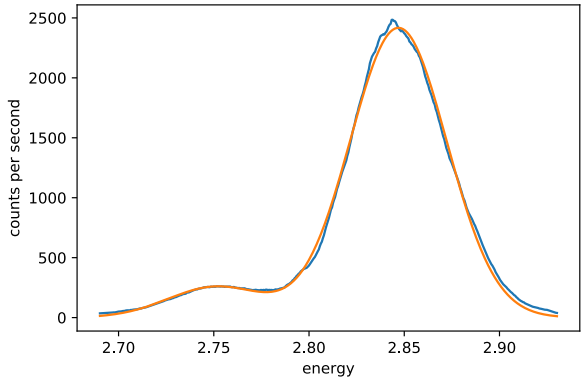

Figure 6.1: PL of the 600nm QDs with a gaussian fit.

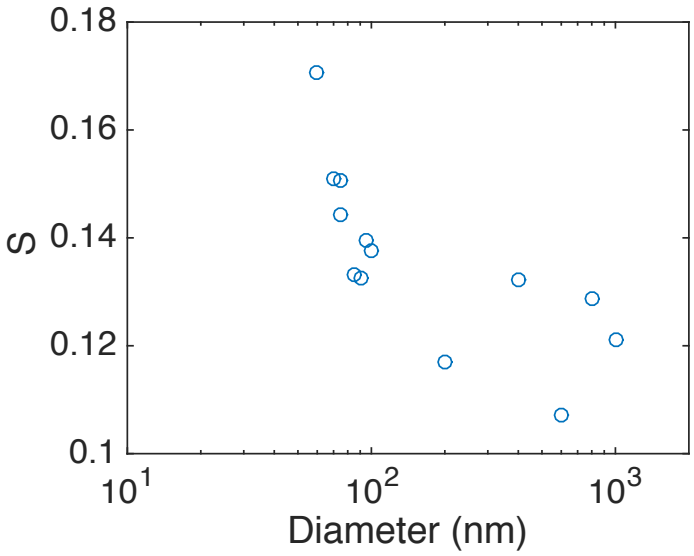

Figure 6.2: Huang-Rhys factor S vs diameter showing the general trend of enhancement of phonon coupling for smaller diameter nanopillars.

The larger diameter nanopillars, which have a lower emission energy, generally correlate with lower phonon coupling strength. This contrasts with previous studies which showed a reduction in phonon coupling with emission energy in quantum wells as a result of either indium concentration or quantum well thickness as mentioned in the previous section. The trend in our data arises because in for nanopillars, a reduction in the piezoelectric field strength in smaller diameter nanopillars is also accompanied by an increase in the lateral confinement (reduced Bohr radius) due to the shrinking diameter. These two effects compete with one another in terms of their effect on the phonon coupling, with the lateral confinement playing a more dominant role in this case. We now lay out a basic model which describes this result.

6.3 Modeling of wavefunction

We model the total wavefunction of electron and hole as [2] [45]:

$$\Phi(\boldsymbol{r_e}, \boldsymbol{r_h}) = N\, f_e(z_e) f_h(z_h) \exp\,(-\rho/\lambda) \qquad (6.3)$$

The parameter λ represents the in-plane localization length/Bohr radius. In this model, the probability dentist function represents the probability of finding the electron and hole laterally separated by ρ and at vertical positions z_e and z_h.

We note that for QWs, it has been noted [46] that theoretically, an increase in the piezoelectric field strength in thick wells should also be accompanied by a decrease in the lateral confinement due to the reduced Coulomb interaction. The separation of electron and hole along z increases S, while the in-plane spreading reduces S. Thus, these two effects compete with one another, with the theoretical value of S eventually decreasing with well thickness for thick enough wells (after showing the opposite trend - S increasing with well thickness- for thin wells).

In order to explain the trend shown in Fig. 6.2, we model the wavefunctions and use the measured S values to determine the localization length λ. In this way our approach is thus similar to that taken in [11]. We model the z-dependence of the QW using an infinite triangular quantum well, with the tilt of the well determined by the diameter-dependent electric field strength. The vertical wavefunction dependence of electron and hole can be understood as arising from the piezoelectric fields whose strength at r = 0 is determined by the aforementioned model. Using calculated values of the electric field at r = 0 as a function of diameter, this allows solutions of the z-dependence of the wavefunctions with solutions given by Airy functions, as shown below.

This approach allows a calculation of λ as a function of diameter. For each diameter, the calculated electric field magnitude for that diameter is used to determine the z-dependent wavefunctions of electron and hole. Then, given S and the z-dependent wavefunctions, the λ

parameter is determined based on Eqn. 6.1. The values of the constants used are $m^*_h = m_0$, $m^*_e = 0.2\ m_0$, $\epsilon_\infty = 5.35$, $\epsilon_0 = 8.9$, $E_{LO} = 91$ meV. Given the measured values of S, we then deduce the corresponding values of λ vs D, as shown in Fig 6.4.

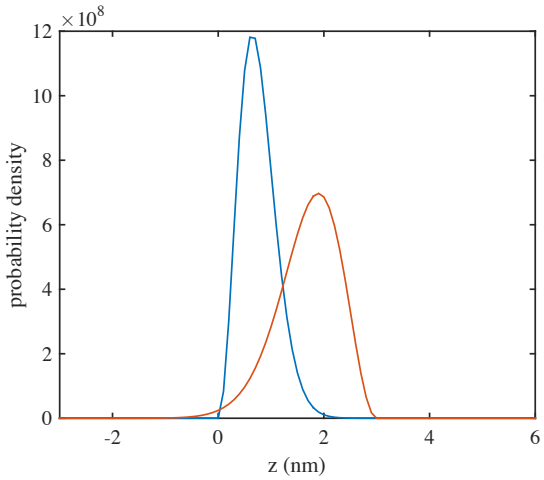

Figure 6.3: Airy function solutions for an infinite triangular quantum well for E = 3.25 MV/cm. This approximation is used to determine the z-dependence of the electron and hole wavefunctions, with E-field varying with diameter.

It may be observed that there is a general reduction of λ with smaller D. Smaller diameter results in reduced piezoelectric fields and thus reduced separation of electron and hole along the z-direction. This effect enhances the Coulomb interaction strength and thus reduce the lateral electron-hole separation λ. Here, the observed lateral confinement/ Bohr radius is observed to decrease from approximately 2.5 nm to 2.0 nm over the observed range of diameters.

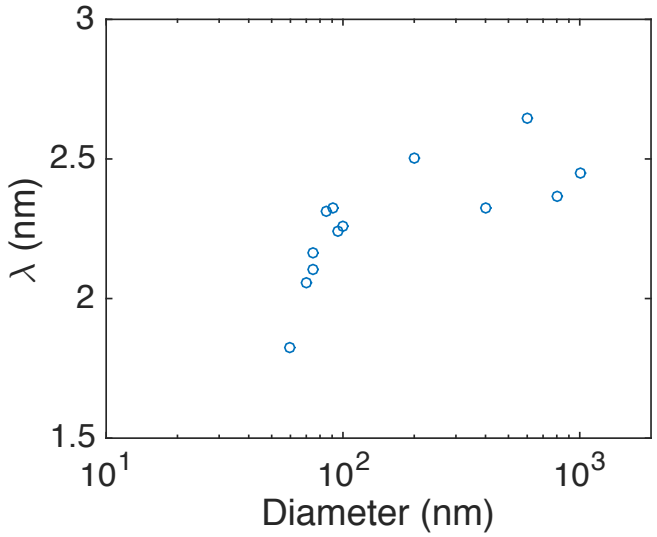

Figure 6.4: λ vs D. There is an increase in localization for small diameter nanopillars. This effect gives rise to the enhancement of phonon coupling for small diameter nanopillars despite a reduction in the piezoelectric fields.

6.4 Summary

Using measurements of the phonon replica strength in the PL of InGaN/GaN QDs in nanopillars of a range of diameters, we find that the smaller nanopillars correspond to a reduced lateral separation of the electron and hole. This effect is quantified using a simple model of the electron and hole wavefunctions and a determination of the vertical component of the wavefunctions using the simulated piezoelectric field strength at the center of nanopillars as a function of diameter. We find that the lateral localization length λ varies from 2 to 2.5nm, with values decreasing for smaller diameter nanopillars. The enhancement of lateral localization for small diameter nanopillars arises due to the reduced vertical separation of electron and hole, which reduces the in-plane Bohr radius of the exciton.

Future work should extend this study to smaller diameter nanopillars. Furthermore, a more detailed analysis would likely require considering the effect of localization due to well width fluctuations and alloying effects of indium. This motivates further study of the effect of

localization in InGaN and its effect on measurable quantities such as phonon coupling strength and other properties affecting practical device performance.

Chapter 7
Effect of nanopillar diameter on Stokes shift in InGaN QDs

In this chapter we report measurements of the Stokes shift in InGaN/GaN quantum disks in nanopillars. This study of this effect as a function of nanopillar diameter allows the relative contributions of the QCSE and localization to be determined. This analysis is enabled by a simple model of the diameter-dependent strain relief in these systems. In section 7.1 we introduce the background of the Stokes shift in InGaN and previous work investigating this topic. In section 7.2 we present measurements of the Stokes shift in InGaN/GaN disks in nanopillars. In section 7.3 we present conclusions.

7.1 Stokes shift in InGaN and physical background

The Stokes shift is the difference between the absorption and emission energies. With regard to InGaN, the nature of the Stokes shift is still being understood. The two main contributions are believed to arise from the quantum confined stark effect (QCSE) and localization due to fluctuations of indium concentration. However, the relative importance of these two effects is often difficult to separate and depends on sample parameters such as average indium fraction and well width.

The existence of the Stokes shift is not unique to nitrides. In GaAs, the Stokes shift depends on sample quality but has been noted in some studies with a magnitude of a few meV of energy shift [47]. In these studies, the Stokes shift was attributed as arising from disorder states for which

the DOS is very low, and which therefore do not contribute significantly to the absorption spectrum. In contrast, in InGaN the Stokes shift is typically enhanced to hundreds of meV and is widely observed, including in very high-quality samples. The physical origins of Stokes shift have been examined by past experimental and theoretical efforts, in connection with several different ideas which we now describe.

The first major explanation of the Stokes shift attributes its origin to a mechanism similar to that described in GaAs, namely localization arising from disorder [48]. One of the reasons this line of thought has motivated so much work is that the very origins of luminescence in InGaN is deeply connected with the role of localization.

The second explanation of the Stokes shift attributes its origin to the role of piezoelectric fields [49]. In an InGaN QW, electrons and holes are pushed to opposite sides of the well by the giant piezoelectric fields. PL typically arises from the ground state due to the ability of carriers to relax to these low-energy states, which are of course red-shifted by the piezoelectric fields. Meanwhile, the fields cause a reduction of the ground state absorption due to the reduced wavefunction overlap, while enhancing the absorption of excited states as their wavefunction overlap becomes relatively enhanced.

Some previous studies have experimentally examined non-polar InGaN/GaN QWs as a means to eliminate the built in fields and so to isolate the effect of localization (well width fluctuations and indium fluctuations) [50]. Similarly, in [51], InGaN/GaN QWs were examined with a comparison of the Stokes shift of a c-plane QW and a semi-polar QW to demonstrate the reduced Stokes shift.

In contrast, here we present an approach which examines our c-plane QW-based samples without requiring parallel measurements of a non-polar QW in order to separate the contributions

of QCSE and Indium fluctuations. As described in the previous chapter, here we study InGaN/GaN quantum disks in nanopillars which have been fabricated by etching a single quantum well into arrays of nanopillars with controlled diameters. The QDs used in this study were fabricated from a 3-nm thick InGaN/GaN quantum well and the QDs measured here were fabricated with diameters ranging from 50nm to 1um as well as the unetched QW.

7.2 Measurements of Stokes shift with InGaN/GaN quantum disks

We use the energy vs. diameter model described in the previous chapter and given by Eqn. 6.2. Note we have $E(D=0) = E_0$ and $E(D)$ asymptotically approaches $E_0 - B_m$ for large diameters. Fitting the energy vs diameter measurements, we obtain E_0, B_m and κ. This is shown in Fig. 7.1. Here we obtain from the diameter-dependent emission energy the strain-relaxed energy $E_0 = 3.158$ eV.

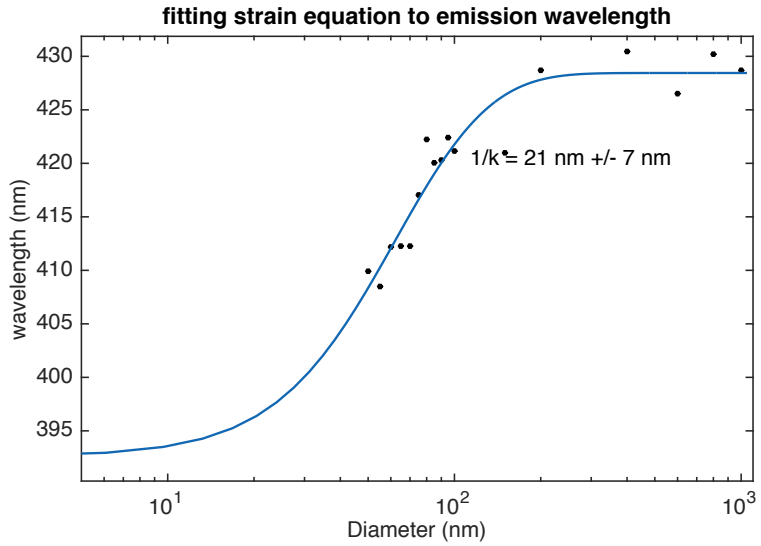

Figure 7.1: Peak PL energy vs diameter. The solid blue curve is the fit to Eqn. (1).

In order to determine the Stokes shift, we measure the absorption using photoluminescence excitation (PLE). Two example PLE spectra shown in Fig. 7.2. As has been previously observed in the literature for InGaN QWs [48], we observe a PLE spectrum that is well fit with a sigmoidal

function and extract E_g. We note E_g is the energy at which the function reaches half of the maximum value:

$$\alpha(E) = \alpha_0 \left(\frac{1}{1 + \exp\left(\frac{E_g - E}{\Delta E}\right)} \right) \tag{7.1}$$

Using these two measurements we then have a measure of the stokes shift for each of six nanopillar diameters including the unetched QW.

In order to separate the contributions to the Stokes shift of QCSE and Indium fluctuations,

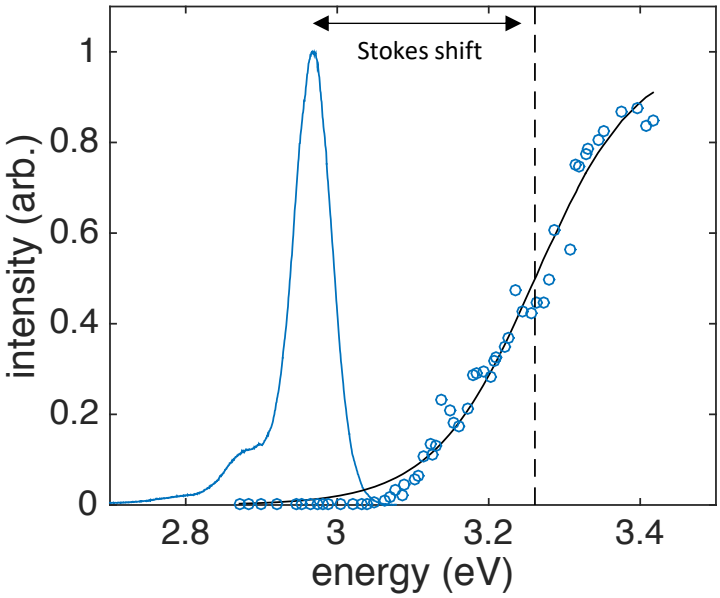

Figure 7.2: PLE spectra and PL for 60nm diameter nanopillars, with the Stokes shift labeled. The black curve is the sigmoidal fit of Eqn. 7.1..

we write $SS(E_{PL}) = SS_{indium} + SS_{PZ}(E_{PL})$. The x-intercept of Stokes shift linear fit should occur near the bandgap energy of pure GaN. At this point, both SS_{indium} and $SS_{PZ}(E_{PL})$ are zero. This has been previously noted and observed using measurements of Stokes shift as a function of indium concentration and of well width. For this data, the Stokes shift reaches an extrapolated value of

zero at E = 3.41 eV. This is a reasonable result, though uncertainty is large, in part because 3.4 eV is rather far from the measured range of emission energies.

We note that for the fully strain-relaxed QD emitting at E_0, there is no QCSE. Thus, the Stokes shift $SS(E_0) = SS_{indium}$. We thus extrapolate the measured Stokes shift out to E_0 in order to quantify the effects of QCSE. We obtain the best estimate of $SS_{indium} = 158 \pm 2$ meV. In fact, this result should be reduced somewhat by the exciton binding energy, though this is a relatively minor

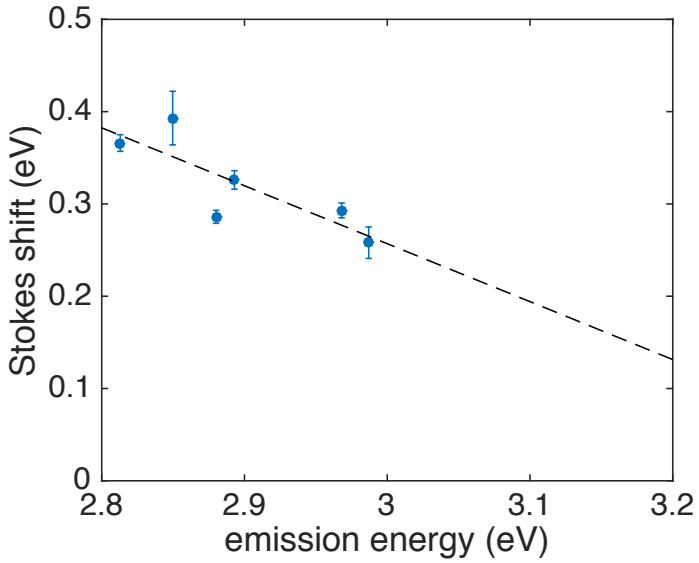

Figure 7.3: Stokes shift vs emission energy for six different diameters nanopillars (including the unetched QW).

contribution. This indicates that for the QW sample, where the total Stokes shift is approximately 350 meV, the contributions of the piezo fields and the indium concentration are of comparable magnitude. As the strain is further relieved with smaller diameters, the contribution to the QCSE becomes relatively smaller and localization dominates the cause of the Stokes shift.

In future studies, power dependent PLE measurements should be carried out to ensure that the laser excitation is at a low enough level to avoid significant screening of the internal fields. Additionally, we note that the effects of localization at well width fluctuations and QCSE are hard

to disentangle. In [14] it was found that electrons localize at well width fluctuations and holes at indium fraction fluctuations. With changing piezoelectric fields, the electron will be affected since with reduced field it will be less localized at the well width fluctuations.

7.3 Summary

In conclusion, we have measured the Stokes shift in InGaN/GaN quantum disks as a function of diameter. Our measurements determine that the total Stokes shift of 350 meV in the unetched QW arises from approximately equal contributions of the QCSE and of localization due to indium fluctuations, and meanwhile the smaller diameters have a reduced stokes shift with smaller effect by the QCSE. This method could permit the study of the contribution of QCSE and stokes shift in InGaN QWs for a range of indium concentration or well thickness, where this same top-down fabrication method could also be employed.

Chapter 8
Conclusions and future work

This thesis studied top-down etched InGaN quantum disks embedded in GaN nanopillars, focusing on the effect of localization and of the exciton-phonon interaction. Understanding of carrier localization in this material is important to addressing the origin of luminescence in InGaN, while an understanding of the exciton-phonon interaction is needed to explain the observed performance limitations such as the green gap and efficiency droop, which are believed to be related to Auger recombination. Additionally, we carried out two studies of nanostructures to demonstrate enhancement of light collection and light emission.

In Chapter 3, we demonstrated that silver plasmonic cavities on InGaN/GaN nanopillars enhanced both the emission intensity and emission rate, as determined using time-resolved photoluminescence. In particular, a plasmonic cavity with an opening at the top of the nanopillar was successfully implemented and allowed for brighter and faster emission of single photon sources than a closed top cavity [52]. In Chapter 4, we demonstrated the effect of nanolenses fabricated onto InGaN/GaN nanopillars. Using a micro-electroluminescence k-space imaging, the enhancement of light collimation by a factor of 1.9x from single nanopillars was demonstrated [24].

In Chapter 5, we studied the effect of asymmetrical strain on the exciton-phonon coupling by examining the optical phonon replica in the PL of nineteen individual elliptical QDs with

dimensions of 22nm x 36nm. We showed that the effect of strain on the phonon coupling strength should be observable by a reduction in the degree of polarization (DOP) of the optical phonon replica. Theoretical calculations of the electron and hole wavefunctions indicated an expected 8% enhancement in the phonon coupling of the x-polarized hole envelope function compared to the dominant y-polarized envelope function. Measurements confirmed that there is a reduction in the DOP of the optical phonon replica, with reasonable agreement with theory for the high DOP dots. Lower DOP dots, which arise to due irregularities in the shape and size of the fabricated nanopillars, also showed a reduction in DOP of the phonon replica but are more sensitive to the effect of asymmetrical phonon coupling and warrant further study. In particular, quantum dots of different aspect ratios and irregular shapes should be studied to determine the agreement of experimental DOP values with theoretical predictions. This could also be useful for applications, as it is possible that novel strain engineering of these nanostructures could result in even higher DOP for some states. Furthermore, the effect of localization such as indium composition fluctuations should be included in the models to accurate describe the electron and hole wavefunctions.

In Chapter 6, we examined the effect of nanopillar diameter on exciton-phonon coupling strength in InGaN quantum disks. We observed an enhancement of the phonon replica as the nanopillar diameter is reduced from 1000nm to 60nm. This effect is explained by a reduction in the lateral Bohr radius of the exciton which accompanies the increase in vertical electron-hole separation in smaller nanopillar diameters. To quantify this effect, a simple model is used to infer that, based on the measured phonon coupling strengths, the Bohr radius reduces from approximately 2.5nm to 2nm as the diameter is reduced over the observed range. Further study could extend this result to smaller nanopillar diameters. An interesting question to address in this area would be the limitations on single photon emission which cause $g^{(2)}(0)$ values to be

significantly greater than zero (while still below the classical limit of $g^{(2)}(0) < 0.5$). Because the exciton binding energy is affected by localization, these effects should play a major role in influencing the ability to excite a single exciton in the system.

In Chapter 7, we study the effect of localization by measuring the Stokes shift as a function of nanopillar diameter. We demonstrate the ability to separately determine the contributions of the strain-induced quantum confined Stark effect and of localization to the observed Stokes shift. In our case, we find that the two effects have approximately equal contributions for the range of nanopillar diameters studied here. This method could be applied to a range of samples for which the nanopillar diameter will provide a useful degree of freedom to study the effects of strain and of localization in determining the Stokes shift. The issue of localization could be further studied by examining the nonradiative relaxation of excited carriers into the localized states. A useful approach in this area would be the use of spectrally resolved time resolved differential transmission measurements, which could investigate the population transfer on picosecond to nanosecond timescales from the excited states into the localized states which are responsible for light emission. This could employ a high energy pump pulse to excite the carriers and a broadband probe pule to measure the time-dependent populations in the lower energy states.

References

[1] I. Vurgaftman and J. R. Meyer, "Band parameters for nitrogen-containing semiconductors," *Journal of Applied Physics*, vol. 94, no. 6, pp. 3675–3696, Sep. 2003.

[2] C. J. Humphreys, "Solid-State Lighting," *MRS Bulletin*, vol. 33, no. 04, pp. 459–470, Apr. 2008.

[3] S. Nakamura, "The Roles of Structural Imperfections in InGaN-Based Blue Light–Emitting Diodes and Laser Diodes," *Science*, vol. 281, p. 7, 1998.

[4] A. A. Setlur, "Phosphors for LED-based Solid-State Lighting," *The Electrochemical Society Interface*, p. 5, 2009.

[5] P. Morgan Pattison, M. Hansen, and J. Y. Tsao, "LED lighting efficacy: Status and directions," *Comptes Rendus Physique*, vol. 19, no. 3, pp. 134–145, Mar. 2018.

[6] J. Y. Tsao, J. Han, R. H. Haitz, and P. M. Pattison, "The Blue LED Nobel Prize: Historical context, current scientific understanding, human benefit," *Annalen der Physik*, vol. 527, no. 5–6, pp. A53–A61, Jun. 2015.

[7] J. Y. Tsao and P. Waide, "The World's Appetite for Light: Empirical Data and Trends Spanning Three Centuries and Six Continents," vol. 6, no. 4, p. 23, 2010.

[8] International Energy Agency, *Light's labour's lost: Policies for Energy-Efficient Lighting*. OECD, 2006.

[9] Tsao, Jeff, "The New World of Lighting: SSL and Beyond," University of Michigan, Ann Arbor, Michigan., 03 31 17.

[10] M. Holmes, S. Kako, K. Choi, P. Podemski, M. Arita, and Y. Arakawa, "Measurement of an Exciton Rabi Rotation in a Single GaN / Al x Ga 1 − x N Nanowire-Quantum Dot Using Photoluminescence Spectroscopy: Evidence for Coherent Control," *Physical Review Letters*, vol. 111, no. 5, Jul. 2013.

[11] D. M. Graham *et al.*, "Optical and microstructural studies of InGaN/GaN single-quantum-well structures," *Journal of Applied Physics*, vol. 97, no. 10, p. 103508, May 2005.

[12] Y. Narukawa, Y. Kawakami, M. Funato, S. Fujita, S. Fujita, and S. Nakamura, "Role of self-formed InGaN quantum dots for exciton localization in the purple laser diode emitting at 420 nm," *Applied Physics Letters*, vol. 70, no. 8, pp. 981–983, Feb. 1997.

[13] C. J. Humphreys, "Does In form In-rich clusters in InGaN quantum wells?," *Philosophical Magazine*, vol. 87, no. 13, pp. 1971–1982, May 2007.

[14] S. Schulz, M. A. Caro, C. Coughlan, and E. P. O'Reilly, "Atomistic analysis of the impact of alloy and well-width fluctuations on the electronic and optical properties of InGaN/GaN quantum wells," *Physical Review B*, vol. 91, no. 3, Jan. 2015.

[15] D. P. Tanner, M. A. Caro, E. P. O'Reilly, and S. Schulz, "Atomistic analysis of the electronic structure of *m* -plane InGaN/GaN quantum wells: Carrier localization effects in ground and excited states due to random alloy fluctuations: Electronic structure of *m* -plane InGaN QWs," *physica status solidi (b)*, vol. 253, no. 5, pp. 853–860, May 2016.

[16] C. M. Jones, C.-H. Teng, Q. Yan, P.-C. Ku, and E. Kioupakis, "Impact of carrier localization on recombination in InGaN quantum wells and the efficiency of nitride light-emitting diodes: Insights from theory and numerical simulations," *Applied Physics Letters*, vol. 111, no. 11, p. 113501, Sep. 2017.

[17] A. Morel, P. Lefebvre, S. Kalliakos, T. Taliercio, T. Bretagnon, and B. Gil, "Donor-acceptor-like behavior of electron-hole pair recombinations in low-dimensional (Ga,In)N/GaN systems," *Physical Review B*, vol. 68, no. 4, Jul. 2003.

[18] B. Monemar, B. J. Ohlsson, N. F. Gardner, and L. Samuelson, "Nanowire-Based Visible Light Emitters, Present Status and Outlook," in *Semiconductors and Semimetals*, vol. 94, Elsevier, 2016, pp. 227–271.

[19] E. Kioupakis, P. Rinke, K. T. Delaney, and C. G. Van de Walle, "Indirect Auger recombination as a cause of efficiency droop in nitride light-emitting diodes," *Applied Physics Letters*, vol. 98, no. 16, p. 161107, Apr. 2011.

[20] Y. C. Shen, G. O. Mueller, S. Watanabe, N. F. Gardner, A. Munkholm, and M. R. Krames, "Auger recombination in InGaN measured by photoluminescence," *Applied Physics Letters*, vol. 91, no. 14, p. 141101, Oct. 2007.

[21] M.-H. Kim *et al.*, "Origin of efficiency droop in GaN-based light-emitting diodes," *Applied Physics Letters*, vol. 91, no. 18, p. 183507, Oct. 2007.

[22] J. Iveland, L. Martinelli, J. Peretti, J. S. Speck, and C. Weisbuch, "Direct Measurement of Auger Electrons Emitted from a Semiconductor Light-Emitting Diode under Electrical Injection: Identification of the Dominant Mechanism for Efficiency Droop," *Physical Review Letters*, vol. 110, no. 17, Apr. 2013.

[23] F. Bassani, G. Pastoria Parravicini, and R. A. Ballinger, *Electronic States and Optical Transitions in Solids*. Pergamon Press, 1975.

[24] B. Demory, K. Chung, A. Katcher, J. Sui, H. Deng, and P.-C. Ku, "Integrated parabolic nanolenses on MicroLED color pixels," *Nanotechnology*, vol. 29, no. 16, p. 165201, Apr. 2018.

[25] A. Nick Vamivakas, Y. Zhao, C.-Y. Lu, and M. Atatüre, "Spin-resolved quantum-dot resonance fluorescence," *Nature Physics*, vol. 5, no. 3, pp. 198–202, Mar. 2009.

[26] K. Chung, J. Sui, B. Demory, C.-H. Teng, and P.-C. Ku, "Monolithic integration of individually addressable light-emitting diode color pixels," *Applied Physics Letters*, vol. 110, no. 11, p. 111103, Mar. 2017.

[27] K. Chung, J. Sui, B. Demory, and P.-C. Ku, "Color mixing from monolithically integrated InGaN-based light-emitting diodes by local strain engineering," *Applied Physics Letters*, vol. 111, no. 4, p. 041101, Jul. 2017.

[28] S.-W. Wang *et al.*, "Wavelength tunable InGaN/GaN nano-ring LEDs via nano-sphere lithography," *Scientific Reports*, vol. 7, no. 1, Dec. 2017.

[29] K. Kishino, K. Nagashima, and K. Yamano, "Monolithic Integration of InGaN-Based Nanocolumn Light-Emitting Diodes with Different Emission Colors," *Applied Physics Express*, vol. 6, no. 1, p. 012101, Jan. 2013.

[30] H.-V. Han *et al.*, "Resonant-enhanced full-color emission of quantum-dot-based micro LED display technology," *Optics Express*, vol. 23, no. 25, p. 32504, Dec. 2015.

[31] H. S. El-Ghoroury, C.-L. Chuang, and Z. Y. Alpaslan, "26.1: *Invited Paper* : Quantum Photonic Imager (QPI): A Novel Display Technology that Enables more than 3D Applications," *SID Symposium Digest of Technical Papers*, vol. 46, no. 1, pp. 371–374, Jun. 2015.

[32] H. S. El-Ghoroury, M. Yeh, J. C. Chen, X. Li, and C.-L. Chuang, "Growth of monolithic full-color GaN-based LED with intermediate carrier blocking layers," *AIP Advances*, vol. 6, no. 7, p. 075316, Jul. 2016.

[33] H.-Y. Lin *et al.*, "Optical cross-talk reduction in a quantum-dot-based full-color micro-light-emitting-diode display by a lithographic-fabricated photoresist mold," *Photonics Research*, vol. 5, no. 5, p. 411, Oct. 2017.

[34] Z. Gong *et al.*, "Matrix-Addressable Micropixellated InGaN Light-Emitting Diodes With Uniform Emission and Increased Light Output," *IEEE Transactions on Electron Devices*, vol. 54, no. 10, pp. 2650–2658, Oct. 2007.

[35] J. Day, J. Li, D. Y. C. Lie, C. Bradford, J. Y. Lin, and H. X. Jiang, "III-Nitride full-scale high-resolution microdisplays," *Appl. Phys. Lett.*, p. 4, 2011.

[36] Zhao Jun Liu, Wing Cheung Chong, Ka Ming Wong, and Kei May Lau, "360 PPI Flip-Chip Mounted Active Matrix Addressable Light Emitting Diode on Silicon (LEDoS) Micro-Displays," *Journal of Display Technology*, vol. 9, no. 8, pp. 678–682, Aug. 2013.

[37] F. Templier, "GaN-based emissive microdisplays: A very promising technology for compact, ultra-high brightness display systems: GaN-based emissive microdisplays," *Journal of the Society for Information Display*, vol. 24, no. 11, pp. 669–675, Nov. 2016.

[38] J. Huang, H.-C. JianJang, and S.-C. Shen, *Nitride Semiconductor Light-Emitting Diodes (LEDs): Materials, Technologies and Applications*.

[39] G. Callsen *et al.*, "Analysis of the exciton–LO-phonon coupling in single wurtzite GaN quantum dots," *Physical Review B*, vol. 92, no. 23, p. 235439, Dec. 2015.

[40] C.-H. Teng, L. Zhang, T. A. Hill, B. Demory, H. Deng, and P.-C. Ku, "Elliptical quantum dots as on-demand single photons sources with deterministic polarization states," *Applied Physics Letters*, vol. 107, no. 19, p. 191105, Nov. 2015.

[41] M. Soltani, M. Certier, R. Evrard, and E. Kartheuser, "Photoluminescence of CdTe doped with arsenic and antimony acceptors," *Journal of Applied Physics*, vol. 78, no. 9, pp. 5626–5632, Nov. 1995.

[42] D. Chen *et al.*, "Enhancement of electron-longitudinal optical phonon coupling in highly strained InGaN/GaN quantum well structures," *Journal of Applied Physics*, vol. 101, no. 5, p. 053712, Mar. 2007.

[43] R. Pecharromán-Gallego, P. . Edwards, R. . Martin, and I. . Watson, "Investigations of phonon sidebands in InGaN/GaN multi-quantum well luminescence," *Materials Science and Engineering: B*, vol. 93, no. 1–3, pp. 94–97, May 2002.

[44] Y. Estrin, D. H. Rich, S. Keller, and S. P. DenBaars, "Observations of exciton–surface plasmon polariton coupling and exciton–phonon coupling in InGaN/GaN quantum wells covered with Au, Ag, and Al films," *Journal of Physics: Condensed Matter*, vol. 27, no. 26, p. 265802, Jul. 2015.

[45] Bastard, Gerald, *Wave mechanics applied to semiconductor heterostructures*. Les Editions de Physique, 1988.

[46] S. Kalliakos *et al.*, "The Effects of Localization and of Electric Fields on LO-Phonon-Exciton Coupling in InGaN/GaN Quantum Wells and Quantum Boxes," *physica status solidi (a)*, vol. 190, no. 1, pp. 149–154, Mar. 2002.

[47] G. Bastard, C. Delalande, M. H. Meynadier, P. M. Frijlink, and M. Voos, “Low-temperature exciton trapping on interface defects in semiconductor quantum wells,” *Physical Review B*, vol. 29, no. 12, pp. 7042–7044, Jun. 1984.

[48] K. P. O’Donnell, R. W. Martin, and P. G. Middleton, “Origin of Luminescence from InGaN Diodes,” *Physical Review Letters*, vol. 82, no. 1, pp. 237–240, Jan. 1999.

[49] A. Hangleiter, J. S. Im, J. Off, and F. Scholz, “Optical Properties of Nitride Quantum Wells: How to Separate Fluctuations and Polarization Field Effects,” *physica status solidi (b)*, vol. 216, no. 1, pp. 427–430, Nov. 1999.

[50] P. Dawson, S. Schulz, R. A. Oliver, M. J. Kappers, and C. J. Humphreys, “The nature of carrier localisation in polar and nonpolar InGaN/GaN quantum wells,” *Journal of Applied Physics*, vol. 119, no. 18, p. 181505, May 2016.

[51] Y. Zhang *et al.*, “Stokes shift in semi-polar (112$\bar{2}$) InGaN/GaN multiple quantum wells,” *Applied Physics Letters*, vol. 108, no. 3, p. 031108, Jan. 2016.

[52] B. Demory, A. Katcher, T. Hill, C.-H. Teng, C. Zhang, L. Guo, H. Deng, and P.-C. Ku, “Improving the Radiative Efficiency of InGaN Quantum Dots via an Open Top Cavity,” *ACS Photonics*, vol. 4, no. 4, pp. 795–799, Apr. 2017.